J. Fluid Mech. (2010), *vol.* 656, *pp.* 82–115. © Cambridge University Press 2010
doi:10.1017/S0022112010001035

Dynamical system approach to instability of flow past a circular cylinder

TAPAN K. SENGUPTA†, NEELU SINGH AND V. K. SUMAN

Department of Aerospace Engineering, Indian Institute of Technology Kanpur, Kanpur 208 016, India

(Received 2 July 2009; revised 21 February 2010; accepted 23 February 2010;
first published online 26 May 2010)

The main aim of this paper is to relate instability modes with modes obtained from proper orthogonal decomposition (POD) in the study of global spatio-temporal nonlinear instabilities for flow past a cylinder. This is a new development in studying nonlinear instabilities rather than spatial and/or temporal linearized analysis. We highlight the importance of multi-modal interactions among instability modes using dynamical system and bifurcation theory approaches. These have been made possible because of accurate numerical simulations. In validating computations with unexplained past experimental results, we noted that (i) the primary instability depends upon background disturbances and (ii) the equilibrium amplitude obtained after the nonlinear saturation of primary growth of disturbances does not exhibit parabolic variation with Reynolds number, as predicted by the classical Stuart–Landau equation. These are due to the receptivity of the flow to background disturbances for post-critical Reynolds numbers (Re) and multi-modal interactions, those produce variation in equilibrium amplitude for the disturbances that can be identified as multiple Hopf bifurcations. Here, we concentrate on $Re = 60$, which is close to the observed second bifurcation. It is also shown that the classical Stuart–Landau equation is not adequate, as it does not incorporate multi-modal interactions. To circumvent this, we have used the eigenfunction expansion approach due to Eckhaus and the resultant differential equations for the complex amplitudes of disturbance field have been called here the Landau–Stuart–Eckhaus (LSE) equations. This approach has not been attempted before and here it is made possible by POD of time-accurate numerical simulations. Here, various modes have been classified either as a regular mode or as anomalous modes of the first or the second kind. Here, the word anomalous connotes non-compliance with the Stuart–Landau equation, although the modes originate from the solution of the Navier–Stokes equation. One of the consequences of multi-modal interactions in the LSE equations is that the amplitudes of the instability modes are governed by stiff differential equations. This is not present in the traditional Stuart–Landau equation, as it retains only the nonlinear self-interaction. The stiffness problem of the LSE equations has been resolved using the compound matrix method.

1. Introduction

Vortex shedding behind a circular cylinder represents flow instability that begins with the growth of disturbances by a linear temporal mechanism followed by nonlinear saturation. This flow has also been identified as an example of a nonlinear dynamical

† Email address for correspondence: tksen@iitk.ac.in

https://doi.org/10.1017/S0022112010001035 Published online by Cambridge University Press

system representing phase transition and instabilities for external flows by Sreenivasan, Strykowski & Olinger (1987) and Provansal, Mathis & Boyer (1987). When this flow is considered as a dynamical system, the transfer function is central with input spectrum playing a residual role at the equilibrium stage. This is the case if the system represents intrinsic dynamics. Huerre & Rossi (1998) refer to this flow as a hydrodynamic oscillator at any post-critical Reynolds number. Here, the criticality refers to the primary temporal instability, which is also described mathematically as a Hopf bifurcation in the parameter space (Golubitsky & Schaeffer 1984).

The idea that the flow represents intrinsic dynamics is also bolstered by the evidential success of Landau's model in explaining supercritical amplitude saturation that is independent of the initial condition. This idea seems to be supported by various numerical studies of the flow in Jackson (1987), Zebib (1987), Morzynski, Afanasiev & Thiele (1999) and Barkley (2006), who have predicted a critical Reynolds number in the range $45 \leqslant Re_{cr} \leqslant 47$. We note that all these simulations by different methods are for a uniform flow over a smooth cylinder.

In real flows, bifurcation initiates with the linear temporal instability and thus the possibility for the flow to be receptive to background disturbances is natural. In such a scenario, the dynamical system acts as an amplifier, and hence input disturbance spectrum is as important as the transfer function. The dependence of criticality upon noise is often lost in the description of theoretical results for stability. However, it stands out when one collates experimental evidences gathered over decades. For example, Batchelor (1988) conjectured Re_{cr} to be between 30 and 40; Landau & Lifshitz (1959) quoted it as 34, based on some unreported experimental observation. Kovasznay (1949) reported $Re_{cr} = 40$, while Roshko (1954) reported a value of 50 for the same. Kiya *et al.* (1982) obtained this value as 52 and Tordella & Cancelli (1991) reported $Re_{cr} = 53$. The sensitive dependence of Hopf bifurcation or instability on facility-dependent disturbances becomes even more evident, when one considers the experimental results of Homann (1936), who showed $Re_{cr} \simeq 65$. These interesting results are also featured in Plate 2 of Batchelor (1988) and in Schlichting (1987, p. 18). Such a high value of Re_{cr} has not yet been satisfactorily explained. In figure 3 of Provansal *et al.* (1987) and figure 6 of Sreenivasan *et al.* (1987), different values of Re_{cr} are reported for cylinders with different length (L) and diameter (D). Similar variations of Re_{cr} were also reported earlier by Nishioka & Sato (1978), and the view expressed in these references is that they are due to different aspect ratios of the models, as the same tunnel was used for the individual experimental cases, i.e. the variations are due to three-dimensionality of the flow field. One notes that the experimental models were fixed from wall-to-wall in the tunnel, specifically, to avoid flow three-dimensionality. However, this claim seemingly contradicts the observation in Williamson (1989) that the flow remains essentially two-dimensional for $Re \leqslant 180$. A higher limit on Re for three-dimensional effects has been obtained in the spectral element calculations of Henderson (1997), where it was reported to be around $Re = 250$. An alternative explanation has been proposed in Sengupta *et al.* (2009*b*), where the authors argued and experimentally demonstrated that the background disturbances in a given tunnel are a strong function of the tunnel speed. Specifically, two cases of $Re = 45$ and 53 were demonstrated using two cylinders with different diameters for each Re (5 mm and 1.8 mm for $Re = 53$, 2.6 mm and 1.8 mm for $Re = 45$) at two different speeds (17 cm s^{-1} and 46.9 cm s^{-1} for $Re = 53$, 26.1 cm s^{-1} and 37.8 cm s^{-1} for $Re = 45$). In both the Reynolds number cases at lower speeds, the background free stream turbulence (FST) at Strouhal frequency was higher by a factor of 10, compared to the corresponding FST level at higher speeds. This difference showed up as a coherent

https://doi.org/10.1017/S0022112010001035 Published online by Cambridge University Press

shedding at the lower speed as opposed to very weak shedding at higher tunnel speeds. This points to the receptivity aspect of the flow field to FST and may be the likely explanation for the different Re_{cr} observed in the experiments of Sreenivasan *et al.* (1987), Provansal *et al.* (1987) and Nishioka & Sato (1978), where different aspect ratio cylinders were used. The variability and coupling between FST and tunnel speed were not explored systematically. The variation of equilibrium amplitude with FST was presented in figure 14 of Sreenivasan *et al.* (1987), which clearly shows a large scatter in the growth rate for Re in the range between 50 and 60. Results for higher FST levels clearly reveal Re_{cr} to be significantly higher than 47. This conundrum of higher Re_{cr} for higher FST levels seems non-intuitive, but will be discussed later in detail, with respect to some calculations for the FST cases. The role of FST can be appreciated by looking at the definition plots for vorticity contours shown in figure 1, for two sets of calculations: zero-FST computations shown in figure 1(b) and with FST level of 0.06 % shown in figure 1(c). Details of FST models and their uses in computing are described in Sengupta *et al.* (2009*b*) and a brief description is also provided here in § 4. In figure 1, same contour levels are plotted for the cases shown that indicate marginal differences in the contour values. The main effect of FST is shown in slightly lower values of vorticity at the cores of the shed vortices, as compared to the zero-FST case. This slight variation can show up as early onset time of primary instability and lower values of Re_{cr}, when the FST levels are low. Effects of higher FST levels are not considered here – those could be significantly different. Some experimental results on the variation of equilibrium amplitude with Re for moderate levels of FST are available in Sreenivasan *et al.* (1987).

So far, the highest value of $Re_{cr} = 65$ has been noted in the experiment of Homann (1936) and it is not certain if this relates to the level of FST that led to a higher critical Reynolds number. However, we also note a particular feature of this experiment. The working medium used in the tunnel was a highly viscous oil that can also effectively damp background disturbances, compared to commonly used fluids like air or water used in other tunnels. Does it imply that the Hopf bifurcation at $Re \simeq 45$ to 47 is bypassed in the experiments of Homann (1936), while it is not prevented above $Re = 65$? One also notes that the experimental results in Strykowski (1986) show a qualitative change in flow between $Re = 60$ and 90. One of the aims of this paper is to provide explanations for these experimental observations. This also provides insight on the existence of multiple modes and their interactions during instability.

Giannetti & Luchini (2007) and Sipp & Lebedev (2007) have also focused on bifurcation in recent times. Global instability associated with flows behaving either as an amplifier or as an oscillator (or resonator) has been studied by Chomaz (2005) and Marquet *et al.* (2008). In Marquet *et al.* (2008), the instability of a recirculating bubble is studied to identify amplifier dynamics with two-dimensional wavepackets localized in the upstream part of the bubble. In contrast, the oscillator dynamics is associated with three-dimensional steady structures. In Chomaz (2005), the open flow dynamics are discussed from a local as well as in the global instability context. According to Chomaz (2005), the 'local and global duality of nonparallel flow instabilities, which, in a way, are analogous to the particle/wave duality underlying the theory of light [or, more generally, quantum mechanics. . . '.

The paper is formulated as follows. In the next section, the governing fluid dynamic equations are provided along with a brief description of the numerical methods used to solve them. This is followed by a detailed description of Hopf bifurcation and the Stuart–Landau equation. In § 4, the role of FST in altering the primary instability and buffeting of the wake is discussed. POD of the spatio-temporal data representing

https://doi.org/10.1017/S0022112010001035 Published online by Cambridge University Press

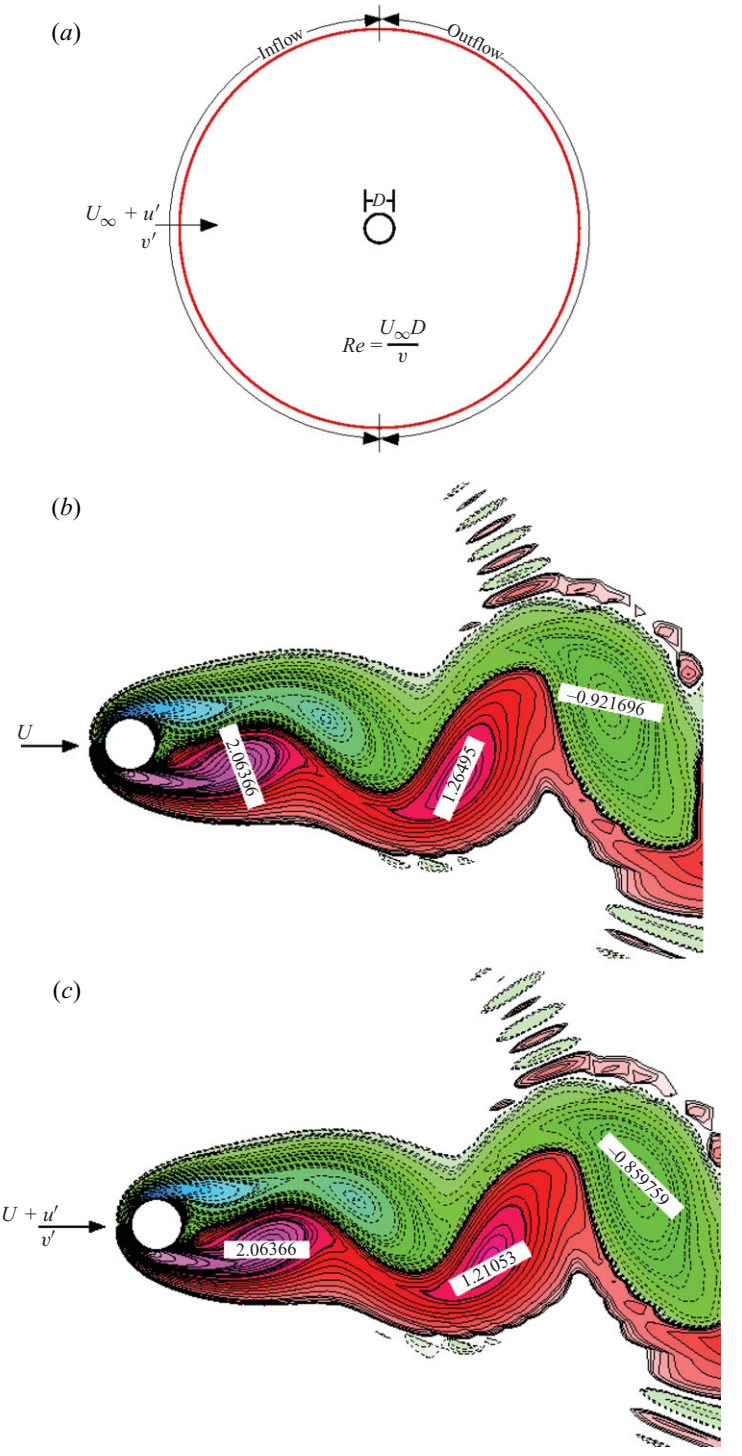


FIGURE 1. (Colour online) (*a*) Schematic of the physical and computational flow field, showing the inflow, outflow and the FST introduced through the inflow. (*b*) Computed vorticity contours for the flow at $Re = 75$, when no FST is introduced through the inflow. (*c*) Computed vorticity contours for the same flow with an FST level given by 0.06 % corresponding to the data of Norberg (2003).

https://doi.org/10.1017/S0022112010001035 Published online by Cambridge University Press

the wake dynamics is performed and analysed in § 5. In § 6, multi-modal interactions governed by the Landau–Stuart–Eckhaus (LSE) equations are studied and compared with the POD results. In addition, the disturbance field is reconstructed using the linear growth/decay rates of leading modes and their interactions. A summary and concluding remarks are given in § 7.

2. Governing equations and numerical methods for simulation of flow past a cylinder

For the numerical simulation of the governing two-dimensional Navier–Stokes equation, the streamfunction vorticity ($\psi - \omega$) formulation is preferred because of its ability to preserve solenoidality of both the unknowns. The introduction of streamfunction as a variable automatically satisfies the divergence-free condition (solenoidality) for the velocity field. This divergence-free condition combined with the pressure–velocity coupling problem is the major source of error in DNS for instability studies using primitive variables. The flow is computed here in an analytical O-grid with 153 points in the azimuthal (ξ) and 400 points in the radial (η) directions, with the outer boundary placed at a distance of 20 diameters from the cylinder surface. Details of the used formulation and the adopted numerical methods are provided in Dipankar, Sengupta & Talla (2007) and Sengupta, Suman & Singh (2010), with only a brief description provided here. The governing equations are written for an orthogonal transformed ($\xi - \eta$) plane:

$$\frac{\partial}{\partial \xi}\left(\frac{h_2}{h_1}\frac{\partial \psi}{\partial \xi}\right) + \frac{\partial}{\partial \eta}\left(\frac{h_1}{h_2}\frac{\partial \psi}{\partial \eta}\right) = -h_1 h_2 \omega, \tag{2.1}$$

$$h_1 h_2 \frac{\partial \omega}{\partial t} + h_2 u \frac{\partial \omega}{\partial \xi} + h_1 v \frac{\partial \omega}{\partial \eta} = \frac{1}{Re}\left[\frac{\partial}{\partial \xi}\left(\frac{h_2}{h_1}\frac{\partial \omega}{\partial \xi}\right) + \frac{\partial}{\partial \eta}\left(\frac{h_1}{h_2}\frac{\partial \omega}{\partial \eta}\right)\right]. \tag{2.2}$$

Here, h_1, h_2 are the scale factors of transformation given by $h_1^2 = x_\xi^2 + y_\xi^2$ and $h_2^2 = x_\eta^2 + y_\eta^2$. The diameter ($D$) of the cylinder is taken as the length scale and free-stream velocity as the velocity scale for non-dimensionalization. The time scale is introduced from these two scales.

The loads (lift and drag) are calculated by solving the pressure Poisson equation (PPE) for the total pressure (P_t). The PPE is obtained by taking the divergence of the momentum equation expressed in primitive variables. For the orthogonal curvilinear coordinate system this equation is given by

$$\frac{\partial}{\partial \xi}\left(\frac{h_2}{h_1}\frac{\partial P_t}{\partial \xi}\right) + \frac{\partial}{\partial \eta}\left(\frac{h_1}{h_2}\frac{\partial P_t}{\partial \eta}\right) = \frac{\partial}{\partial \xi}(h_2 v\omega) - \frac{\partial}{\partial \eta}(h_1 u\omega). \tag{2.3}$$

The no-slip boundary condition on the cylinder wall is satisfied by

$$\left.\frac{\partial \psi}{\partial \eta}\right|_{body} = 0. \tag{2.4}$$

An additional condition arising out of the no-slip condition is given by

$$\psi = \text{constant}. \tag{2.5}$$

This condition is used to solve (2.1), while both (2.4) and (2.5) are used to evaluate the wall vorticity (ω_b) that provides the boundary condition to solve (2.2). At the outer boundary (i) a uniform flow condition is applied at the inflow (Dirichlet condition on ψ for the upstream part of the outer boundary) and (ii) a convective boundary

https://doi.org/10.1017/S0022112010001035 Published online by Cambridge University Press

condition is applied for the radial velocity at the outflow. Through the outflow part of the boundary, shed vortices depart the computational domain smoothly, without affecting the flow inside the domain. The radiative condition applied at the outflow is given by

$$\frac{\partial u_r}{\partial t} + u_c(t)\frac{\partial u_r}{\partial r} = 0, \tag{2.6}$$

where u_r is the radial component of velocity and $u_c(t)$ is the convection velocity at the outflow at time t, obtained from the radial component of velocity at the previous time step, i.e. $u_c(t) = u_r(t - \Delta t)$. The initial condition is given by the potential flow, for the impulsive start of the cylinder from rest.

While solving (2.2), the nonlinear convection terms are discretized using a high-accuracy DRP scheme of Sengupta, Sircar & Dipankar (2006) that provides near-spectral accuracy. A second-order central differencing scheme is used for the Laplace operator and a four-stage Runge–Kutta integration scheme is used for time-marching. A sixth-order non-periodic filter is applied on the vorticity field to remove spurious disturbances due to aliasing and other nonlinear numerical instability problems, with the details on filters given in Sengupta, Bhumkar & Lakshmanan (2009*a*).

The location of upstream boundary can contribute significantly to the accuracy of the computed solutions, as reported in appendix A of Sipp & Lebedev (2007). A detailed discussion on various numerical approaches in the literature is given in Giannetti & Luchini (2007), who have used immersed boundary method to avoid committing additional errors due to aliasing via discretization of dissipation. Working in a Cartesian grid avoids aliasing error committed in discretizing dissipation terms in the transformed plane. The use of Cartesian grids can bring in additional issues of interpolation at the solid boundary, and forcing terms are necessary in mass and momentum conservation equations. Issues related to interpolation errors have been discussed in detail in Sengupta *et al.* (2010) and other references given therein. In contrast, we have used a high-accuracy compact scheme in the transformed plane, as reported in Sengupta *et al.* (2006, 2010) and Dipankar *et al.* (2007) for this problem. The choice of time-integration method is also another source of numerical problem. If one uses more than two time levels, additional spurious mode(s) are invoked. Such modes siphon off the high-frequency components of the initial condition, which are removed subsequently during time marching; see the discussion in Sengupta *et al.* (2006) for further details. For problems of flow instability, transition and turbulence, this could be a major source of error, as chaotic dynamical systems are sensitively dependent upon the initial condition. Hence, removal of a component of the initial condition by spurious modes can alter the dynamics qualitatively and quantitatively. Here, to avoid this pitfall, we have used a fourth-order accurate, two-time-level Runge–Kutta method that does not suffer from this problem. Also, for a higher accuracy of the numerical solution, we will be able to reconstruct the POD mode amplitudes with unprecedented accuracy.

Discretized Poisson equations are solved using the Bi-CGSTAB variant of the conjugate gradient method of Van der Vorst (1992). Solving (2.3) requires the Neumann boundary condition on the physical surface and at the far field and these are obtained from the normal (η) momentum equation given by

$$\frac{h_1}{h_2}\frac{\partial P_t}{\partial \eta} = -h_1 u\omega + \frac{1}{Re}\frac{\partial \omega}{\partial \xi} - h_1\frac{\partial v}{\partial t}. \tag{2.7}$$

https://doi.org/10.1017/S0022112010001035 Published online by Cambridge University Press

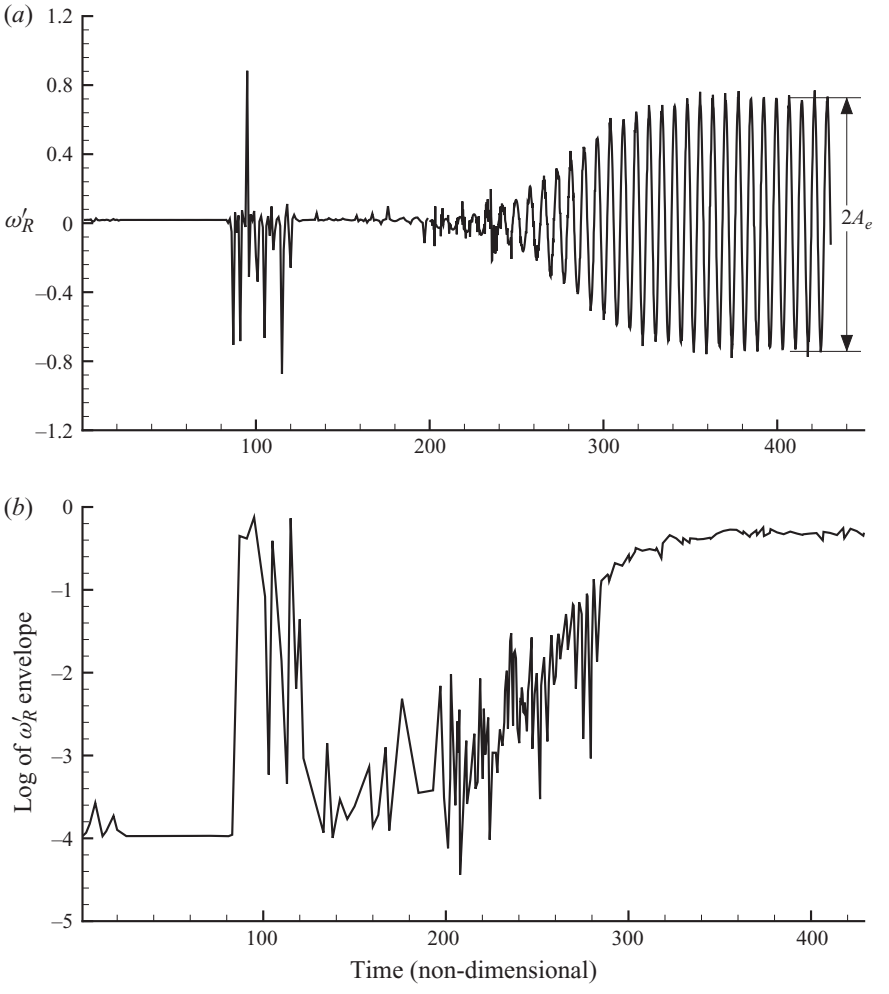


FIGURE 2. For caption see facing page.

Computational results for the flow past a cylinder are shown in figure 2(*a*,*b*). Time variation of vorticity at a near-wake point R ($x_R = 0.5044$, $y_R = 0.0$) with respect to the centre of the cylinder is shown in the top frame for $Re = 60$. At the bottom frame, we have shown the logarithm of the envelope of the amplitude. In figure 2(*c*,*d*), experimental results from Strykowski (1986) for $Re = 49$ are shown for the streamwise fluctuating velocity component. For the experimental conditions, the time in seconds has to be scaled up by a factor of 378.43 to obtain the corresponding non-dimensional time. For both these Reynolds numbers, the effects of transients during the process of linear instability play a major role and are compared here. The slope of the envelope provides the linear temporal growth rate of a normal mode, only if the amplitude of the disturbance is small enough to neglect the contributions due to other modes and their nonlinear interactions. A strong similarity in trend between experimental and computational results shows the accuracy of the numerical methods used here. Interested readers are referred to Sengupta *et al.* (2010) for details of the methods used. If there were only a single dominant mode present, then the time variation would appear initially as an exponentially growing curve

https://doi.org/10.1017/S0022112010001035 Published online by Cambridge University Press

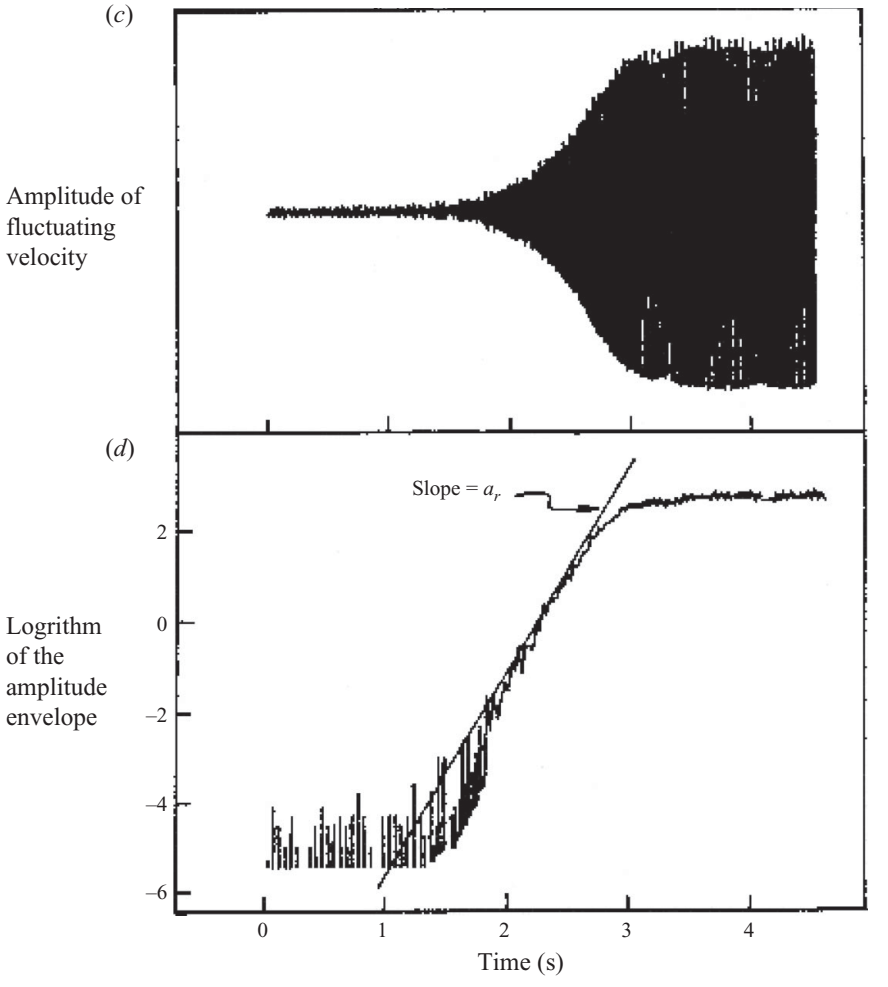


FIGURE 2. (a,b) Computed time variation of vorticity at the near-wake point R ($x_R = 0.5044$, $y_R = 0.0$) shown for $Re = 60$ (a) along with its envelope (b). (c,d) Experimental data from Strykowski (1986) for fluctuating velocity (c) and the logarithm of the amplitude envelope (d) for $Re = 49$. Note that the dimensional time of 1 s in (c,d) is equivalent to 378.435 of the non-dimensional time.

(when the amplitude is small), which would finally culminate in a time-independent amplitude after the nonlinear 'saturation' stage has reached. However, the variation of 'saturation' amplitude from cycle to cycle indicates the presence of more than one dominant mode. This variation of 'equilibrium amplitude' is seen unmistakably in both the experimental and computational results.

Accuracy of the present computations can also be noted by comparing the numerical results with the available experimental results for fluctuating quantities. In figure 3(a), the computed equilibrium amplitude of the lift coefficient is plotted against Reynolds number as discrete symbols. We note that the equilibrium value is the average of amplitudes calculated over a long time interval for each Reynolds number case, after the nonlinear 'equilibrium stage' in the evolution of lift coefficient is reached. In the figure, the correlation obtained analytically by Norberg (2003), based on experimental data, is shown by the continuous line. Computed results show that the discrete points

https://doi.org/10.1017/S0022112010001035 Published online by Cambridge University Press

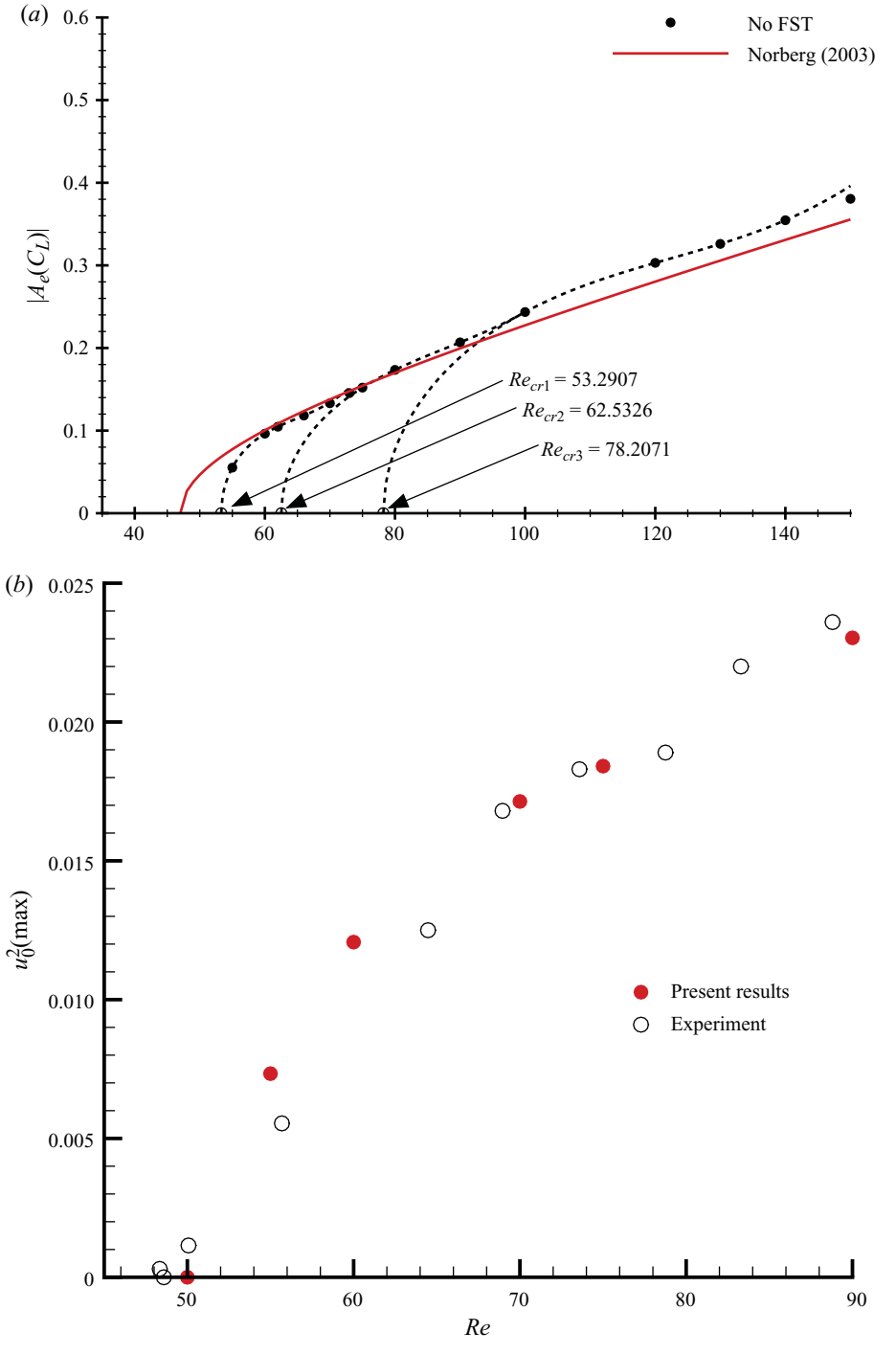


FIGURE 3. (Colour online) (*a*) Equilibrium amplitude of fluctuating lift variation plotted against Reynolds number, using peak-to-peak computed data, and the experimental correlation shown is from Norberg (2003). (*b*) Experimental data (blank circle) from Strykowski (1986) and present computation (filled circle) showing variation of amplitude of fluctuating streamwise velocity component with Reynolds number. The data were obtained at 8 diameter behind the cylinder in the wake. The present computed data have been normalized with the experimental value for $Re = 70$.

https://doi.org/10.1017/S0022112010001035 Published online by Cambridge University Press

do not fall on a single smooth curve; despite this, the match between the analytical fit of Norberg (2003) and present computations is very good. The data in Norberg (2003) were obtained by a single analytical function for a tunnel with a turbulent intensity $Tu = 0.06\,\%$, while the computational data are affected by very low levels of numerical noise of the high-accuracy method. Present computations also produce strikingly similar results with the experimental results taken from Strykowski (1986) in figure 3(*b*), where the mean square streamwise disturbance velocity data are shown as a function of Re.

3. Hopf bifurcation and flow instability

Uniform flow past a circular cylinder experiences a Hopf bifurcation, taking it from a stationary to a time-periodic state for the disturbances in the wake. Having identified the first bifurcation as due to the linear instability mechanism, it is easy to understand that the flow behaves like an amplifier at these lower Reynolds numbers. During the instability, disturbance velocity can be represented as given in Drazin & Reid (1981) as

$$u'(\boldsymbol{X}, t) = \sum_{j=1}^{\infty} \left[A_j(t) f_j(\boldsymbol{X}) + A_j^*(t) f_j^*(\boldsymbol{X}) \right], \tag{3.1}$$

where $\{f_j\}$ is any complete set of complex space-dependent functions satisfying boundary conditions. In (3.1), quantities with asterisks denote complex conjugates. If the complex amplitude is given by $A_j(t) = (\text{constant})\, \mathrm{e}^{s_j t}$, then the individual modes are seen to be governed by $\mathrm{d}A_j/\mathrm{d}t = s_j A_j$, in the early stage of disturbance growth. This is the usual approach taken in the linear normal mode eigenvalue analysis, with the attendant assumption that each mode influences the flow independently. For this flow beyond the exponential growth stage, the disturbance field saturates via nonlinear actions. In the normal mode approach, if one considers only a single dominant mode, then the nonlinear saturation was explained by Landau (1944) in the amplitude evolution equation by considering only the nonlinear self-interaction, i.e.

$$\frac{\mathrm{d}|A|^2}{\mathrm{d}t} = 2\sigma_r |A|^2 - l_r |A|^4, \tag{3.2}$$

where $s_j = \sigma_r + \mathrm{i}\omega_1$ and l_r is the real Landau coefficient. Note that Landau (1944) did not address the issue of phase of the disturbance field and (3.2) was proposed as a model without rigorous derivation. Subsequently, Stuart (1960) developed a satisfactory differential equation for a plane parallel flow following the mathematical foundation in Watson (1960), by retaining only the first term of a series solution. In this formalism, the Landau coefficient is a complex quantity ($l = l_r + \mathrm{i}\, l_i$) and the phase equation is additionally obtained as

$$\frac{\mathrm{d}\theta}{\mathrm{d}t} = \omega_1 - \frac{l_i}{2} |A|^2, \tag{3.3}$$

where $A = |A| \mathrm{e}^{\mathrm{i}\theta}$ and the amplitude equation remains the same as given in (3.2). These two equations together are referred to as the Stuart–Landau equation, for a single dominant mode with nonlinear self-interaction. In the literature, variations of the Stuart–Landau equation are considered as in Provansal *et al.* (1987), Sreenivasan *et al.* (1987), Sipp & Lebedev (2007), Dusek, Le Gal & Fraunie (1994), Thompson & Le Gal (2004) and Noack *et al.* (2003). According to Sipp & Lebedev (2007), some of these works 'did not consider A as amplitude of any global structure, but only as

https://doi.org/10.1017/S0022112010001035 Published online by Cambridge University Press

a scalar variable (like a velocity component) taken at a particular point in the flow'. In figure 3(*a*), a computational result for the equilibrium amplitude of fluctuating lift coefficient is presented. We would get an identical time variation if vorticity was plotted instead. This is because the lift is directly proportional to the area integral of vorticity and is an attribute of global temporal instability suffered by such flows. Experimental data taken from Strykowski (1986) are shown in figure 3(*b*) for the squared streamwise displacement velocity at a fixed location. A strong qualitative similarity between the experimental and computational results shows a global analysis based on DNS will be able to obtain the correct spatial structure of global modes and the Landau coefficient will be the same for every point in the domain.

The presence of more than one dominant mode in the nonlinear saturation stage has led to attempts in explaining wake dynamics of cylinders by POD of numerically simulated data by empirical Galerkin models. Pioneering efforts for this specific flow problem, following the methodologies given in Kosambi (1943), Sirovich (1987) and Holmes, Lumley & Berkooz (1996), are due to Deane *et al.* (1991) and Ma & Karniadakis (2002) for two- and three-dimensional wakes, respectively. In contrast, Noack & Eckelmann (1994) followed the carrier-field ansatz of Zebib (1987) for the mathematical Galerkin model satisfying completeness of the basis functions requiring hundreds of global eigenmodes. In the context of flow evolution in the cylinder wake during the transient stage of flow instability, the presence of transients was studied by Noack *et al.* (2003), with a goal to provide a hybrid approach combining the 'strengths of empirical and mathematical Galerkin models'. The essence of this was to introduce an additional mode termed the shift mode. This idea has been further extended in Noack *et al.* (2009) and Tadmor *et al.* (2010), and according to these authors 'a key deficiency of both standard POD models and of linearization-based models, is the exclusion of the interaction of oscillatory unsteadiness with the mean flow.... It eludes linear stability analysis and (linear) balanced POD constructions, due to the intrinsic nonlinearity of the interactions of the unsteady fluctuations with the mean field.' Introduction of the shift mode in Noack *et al.* (2003) was to incorporate this nonlinear dynamical effect of the mean-field correction during the transient stage. This is constructed from the steady solution and the time-averaged flow for $Re = 100$, as shown in figure 7 of Noack *et al.* (2003). We note that the shift mode has a top-down symmetry about the wake centreline. Introduction of the shift mode is equivalent to splitting the unsteady Navier–Stokes equation into a time-averaged mean field as affected by the time-dependent perturbation field via a wave-induced stress that couples the two fields. Unlike the classical Reynolds stress characterized by hydrodynamic turbulence, this wave-induced stress can be obtained by phase averaging (or ensemble averaging). Note that phase averaging can take care of one mode at a time in building up the additional stress that goes into the mean-field correction. However, ensemble averaging will be computationally intensive – more time would be required for this than solving the full Navier–Stokes equation from first principles. It is already noted in Noack *et al.* (2003) that the 'price for efficient low-dimensional description of the reference simulation is a low accuracy for transients'. In the present exercise, the direct simulation of the Navier–Stokes equation is used to study the wake dynamics by using different analytical tools. Such an approach will not only include the effects of the shift mode but would also have multi-modal interactions built into the solution. In figure 2, one notices the presence of multiple modes after the nonlinear saturation following the initial exponential growth. In this work, we have provided an augmented Stuart–Landau equation, including the interactions of active modes, aided by the DNS results.

https://doi.org/10.1017/S0022112010001035 Published online by Cambridge University Press

Despite the nonlinearity of (3.2), it is directly integrable to (Drazin & Reid 1981)

$$|A|^2 = \frac{A_0^2}{(A_0/A_e)^2 + [1 - (A_0/A_e)^2]\ \mathrm{e}^{-2\sigma_r t}}, \tag{3.4}$$

where A_0 is the value of A at $t = 0$. Here, $A_e = \sqrt{2\sigma_r / l_r}$ represents the asymptotic value of the solution for $t \to \infty$. The condition $\sigma_r > 0$ corresponds to the case when the Reynolds number exceeds Re_{cr} for linear instability. The approach of A to A_e indicates independence of A_e on A_0, a reason for which this flow is considered as an oscillator. Such a solution is due to particular combination of the real part of the Landau coefficient being positive and $Re > Re_{cr}$ that takes the temporally growing flow to a strictly time-periodic neutral state of 'supercritical stability'. For supercritical Reynolds numbers, $\sigma_r \sim (Re - Re_{cr})$, and thus a plot of A_e versus Re will represent a parabolic variation between the two. It is noted that the Stuart–Landau model has better applicability near Re_{cr} (see Drazin & Reid 1981) and it is tested furthermore in the present analysis.

Figures 3(a) and 3(b) display existence of a discontinuous variation of A_e with Re for the experimental and computational data, which in turn indicates the existence of more than one dominant mode during the flow instability and its subsequent nonlinear saturation. In figure 3(a), we have also shown the analytic correlation by Norberg (2003) based on experimental data from a single wind tunnel. It is generally believed that all these displayed variations originate via a Hopf bifurcation following Stuart–Landau equation (3.2). But the discontinuities in the figures are due to either the presence of multiple modes responsible for different Reynolds numbers or their continuous presence at all Reynolds numbers, with different interactions for different Reynolds number ranges. This behaviour, seen in experiments and computations, can also be due to a combination of both these effects simultaneously. However, the discontinuous variation is indicative of more than one leading mode and one bifurcation, as is commonly modelled through Stuart–Landau equation. One can interpret the A_e versus Re curve to begin with the first Hopf bifurcation, and there is a second bifurcation originating at yet higher Reynolds number, with the segments merging at the discontinuities. Computational data in figure 3(a) shown by discrete symbols indicate the presence of two such discontinuities to originate from three bifurcations.

An analysis is performed here for the bifurcation sequence noted for the flow in figures 3(a) and 3(b). To our knowledge, this has not been done before for this flow. For the experimental data shown in figure 3(b), a discontinuity is clearly noted near $Re = 80$, and our computed results in figure 3(a) reveal a similar discontinuity for Re above 75. According to Stuart–Landau model, this curve should have been strictly parabolic, while we have fitted quartic polynomials for the computed data in different ranges of Reynolds numbers according to

$$|A_e|^2 = k_{1i} Re + k_{2i} Re^2 + k_{3i} Re^3 + k_{4i} Re^4, \tag{3.5}$$

where Re_{cri} is the critical Reynolds number in the appropriate ranges, as defined in table 1. The values for the equilibrium amplitude (A_e) obtained from DNS for different Reynolds numbers are used in (3.5) for the first four points in each range of Reynolds numbers indicated in the first column of table 1. Having obtained k_{ij} constants in different ranges, they are used in (3.5) to draw the dotted lines as shown in figure 3(a). In the figure, wherever the dotted line in each segment intersects the Reynolds number axis, that point defines the corresponding Re_{cri} of that range and are listed in the last column of table 1. The primary intention here is to show the proximity of the value

https://doi.org/10.1017/S0022112010001035 Published online by Cambridge University Press

Re range	$k_{1i} \times 10^2$	$k_{2i} \times 10^4$	$k_{3i} \times 10^5$	$k_{4i} \times 10^8$	Re_{cri}
53.29–75	−2.0256	9.34156	−1.4345	7.4092	53.2907
62.53–100	−0.9750	3.3070	−0.3667	1.3940	62.5326
78.20–150	−1.1630	2.9389	−2.3580	0.6414	78.2071

TABLE 1. Coefficients used in the saturation amplitude equation given by (3.5).

of Re_{cr2} for the second bifurcation with the Reynolds number for vortex shedding in Homann (1936) and the kink noted in the (A_e versus Re) curve in Strykowski (1986), as reproduced in figure 3(b). We also note that though (3.5) represents a quartic, the cubic and quartic terms are of lesser importance. Thus, comparisons in figures 2 and 3 not only establish the accuracy of the computed results here but also support the higher critical Reynolds number observed in Homann (1936), which is a direct attribute of multiple Hopf bifurcations for this flow field.

We note that Noack *et al.* (2003) also have reported their computed A_e versus Re using a Galerkin model, without and with the shift mode (models A and B, respectively). Figure 12 of Noack *et al.* (2003) reports a very interesting result. Model B reports a Hopf bifurcation at $Re = 47$, while model A reported $Re_{cr} \simeq 80$, which was also reported by Deane *et al.* (1991) using a similar model. Thus, the shift mode is shown to be central in calculating the correct Re_{cr}. Presented results using DNS automatically include the effects of the shift mode and despite that the first Hopf bifurcation is indicated at higher Reynolds number than that predicted by many other researchers. The reason must lie elsewhere, as different experimental facilities report different critical Reynolds number because of different extant background noise environment, and this aspect has not been investigated theoretically or computationally. The effects of FST in determining Re_{cr} are studied next to address this issue.

4. Role of free-stream turbulence in determining critical Reynolds number

In real flows, omnipresent FST with low amplitude of excitation triggers transition to turbulence that would be essentially different from that predicted by computations of a uniform flow over smooth geometries. FST, in general, appears as a random event that is often modelled stochastically. However, in Sengupta *et al.* (2009*b*), a new approach to model FST has been introduced, where a combination of deterministic and stochastic approaches have been advanced and used in computing. Other efforts in modelling FST are recounted in Sengupta *et al.* (2009*b*). In proposing the model for FST, it is noted that for the statistical description of turbulence, the variance or the second-order statistics represents the magnitude of turbulence fluctuations, skewness or the third-order statistics represents deviation from symmetric distribution and kurtosis or the fourth-order statistics describes the flatness of the tail of the distribution. In experiments, low-frequency deterministic sources are present inherently due to the design of facilities and have to be incorporated. One such model has been developed and used in Sengupta *et al.* (2009*b*), which is reproduced in figure 4(a) comparing data from one wind tunnel facility with the corresponding data generated by the developed synthetic FST model. It is evident that low-frequency components of FST match quite well. Computational results of flow past a cylinder for $Re = 55$ were also reported in Sengupta *et al.* (2009*b*), using this FST model to show the comparison with results of Homann (1936).

https://doi.org/10.1017/S0022112010001035 Published online by Cambridge University Press

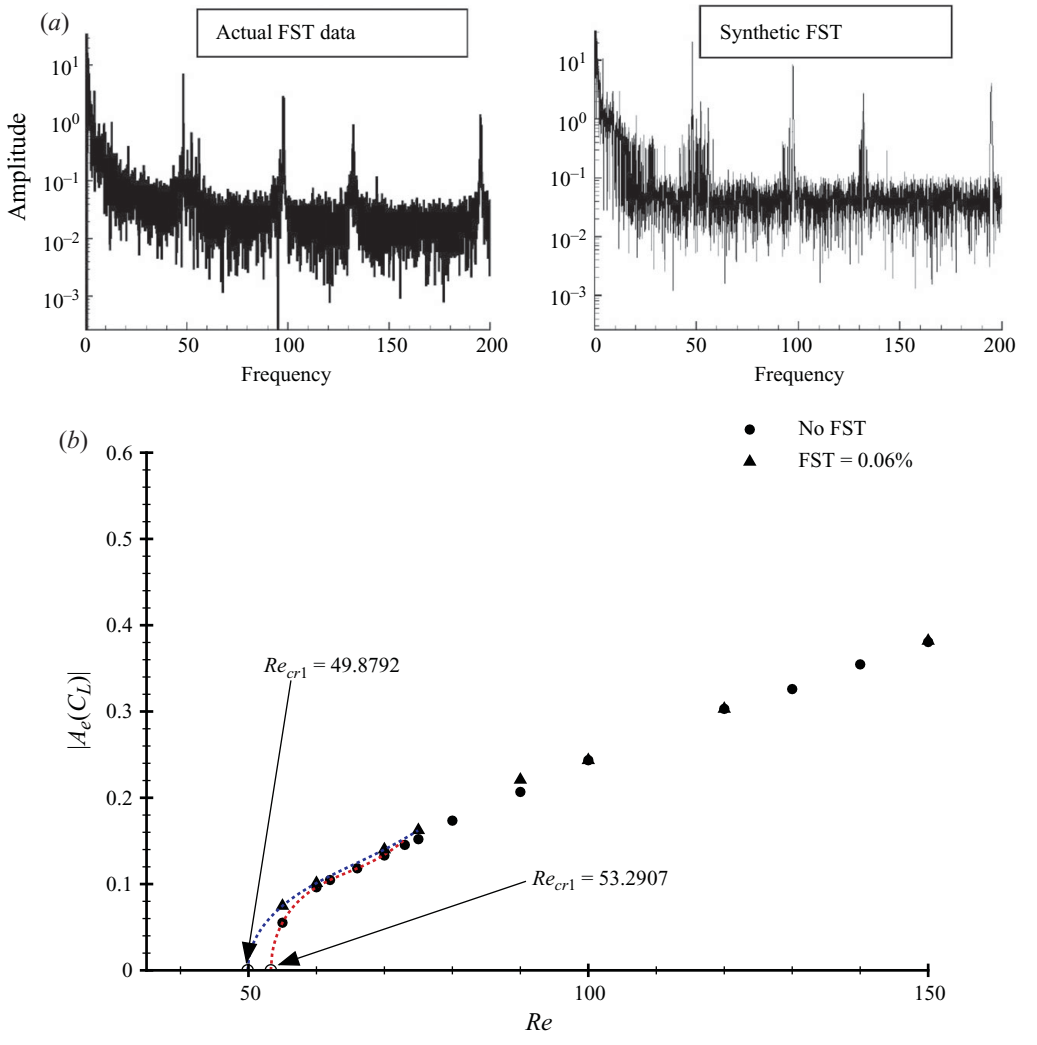


FIGURE 4. (Colour online) (*a*) FFT of actual and modelled FST data obtained using (4.1). (*b*) Comparison of equilibrium amplitudes of fluctuating lift variation plotted against Reynolds number for cases without and with FST level of $Tu = 0.06\,\%$ corresponding to the case of Norberg (2003).

The FST is parametrized using a moving average model of order one, in which a time series is created for the streamwise disturbance component of the velocity field represented by (Sengupta *et al.* 2009*b*)

$$u' = e_t + \alpha e_{t-1} + \sum_{j=1}^{N} a_j \mathrm{e}^{\mathrm{i}k(x-ct)}, \tag{4.1}$$

where the first two terms are given by a Gaussian distribution at successive time steps with a standard deviation (σ) and the last term represents low-frequency component of the FST that is facility- and speed-dependent; c is the phase speed of the propagation of the low-wavenumber coherent structures. Such a model is used at the inflow of the computational domain to provide the background disturbance for solving the Navier–Stokes equation as shown in figure 1. Sengupta *et al.* (2009*b*) noted that the

https://doi.org/10.1017/S0022112010001035 Published online by Cambridge University Press

exact value of c is not very important. Thus, at every time step of integrating the VTE (2.2), input disturbance field is obtained by using (4.1) for every point of the inflow.

The above FST model has been used to compute a flow field for a turbulence intensity (Tu) of 0.06 %, a value for the wind tunnel used in Norberg (2003). The receptivity aspect of flow past a circular cylinder has not yet been investigated in a systematic manner and this is one of the motivations for the present exercise. In figure 4(b), we have compared the computed A_e versus Re curves between the cases of zero FST and $Tu = 0.06\,\%$ to essentially highlight the difference for the first Hopf bifurcation. The same procedure is used, i.e. fitting a quartic relation between A_e^2 and Re, as given in (3.5). With the introduction of a small level of FST, Re_{cr1} comes down from 53.2907 to 49.8792, and this can explain why different experimental facilities report different critical Reynolds numbers. This helps one understand the role of numerical noise in reporting Re_{cr} by different numerical methods or by using the same method with different numerical parameters. This also helps one realize that the qualitatively different value of Re_{cr} in Homann (1936) is due to the totally different working medium used in the experiment. It is consistent with the reported result in Sengupta *et al.* (2009*b*), where it has been established experimentally that two flows with the same Reynolds number can differ because of a different background noise environment. During the receptivity stage of the corresponding linear instability, such dependence on input disturbance is obvious. Control of primary instability can be achieved by changing the working medium as in Homann (1936), where the highly viscous oil used as the working medium contributed to effective dissipation of background disturbances.

5. Proper orthogonal decomposition of flow past a cylinder

POD expansion was originally developed by Kosambi (1943) using the fact that complex stochastic spatio-temporal dynamics can be projected onto a deterministic eigenfunction set. Major works using POD related to stochastic fluid mechanics and specifically to turbulent flows have been described in Holmes *et al.* (1996). The POD technique that is used most often is the method of snapshots due to Sirovich (1987). Another alternative is given in Sengupta & Dey (2004) in the context of reduced order modelling by locating eigenvalues and eigenvectors of the covariance matrix using Lanczos iteration. We report results here based on the method of snapshots.

In many fluid flow problems including the one considered here, coherent structures in the flow can be defined with the help of POD using the method of snapshots of Sirovich (1987). This is most useful when the spatio-temporal dynamics are not affected by stochastic components and one is looking to develop a physical model for such a dynamical system as attempted here. In this method, the number of snapshots M used for the analysis is significantly smaller than the number of grid points used. Data obtained by DNS provide the ensemble of snapshots taken at M instants of time. Taking a reduced number of basis functions (from the complete set in a separable Hilbert space) causes the mathematical modes to be projected as empirical modes.

In performing POD analysis, we choose a time horizon over which a time mean is sought, and this is subtracted from the instantaneous quantity to get the fluctuating component of the field. Velocity fields are often used for POD analysis, so that the cumulative sum of the eigenvalues provides a measure of the kinetic energy. But, in the present work (as well as in Sengupta & Dey 2004, Dipankar *et al.* 2007, Sengupta *et al.* 2010) we have used the vorticity field, so that the eigenvalues provide a measure

https://doi.org/10.1017/S0022112010001035 Published online by Cambridge University Press

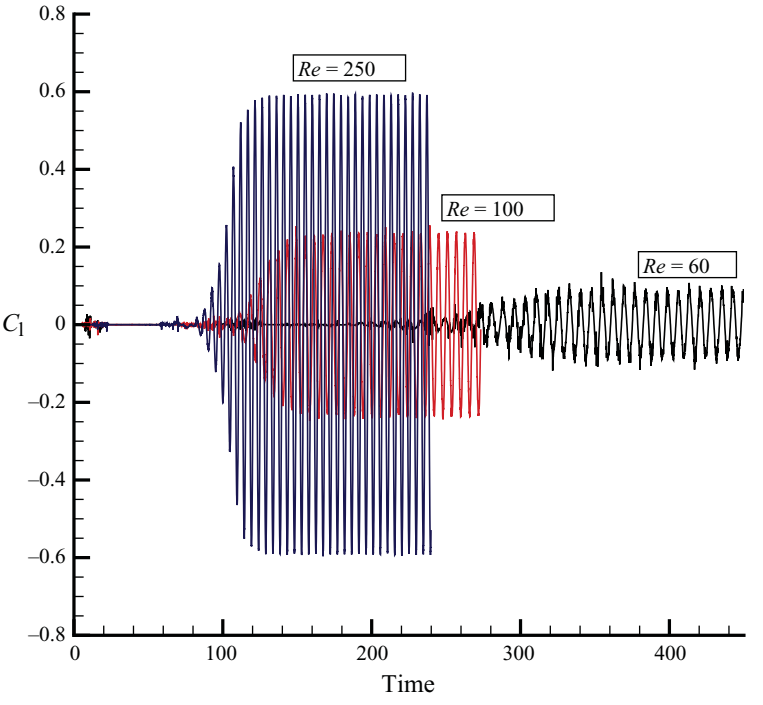


FIGURE 5. (Colour online) Computed lift coefficient variation with time for $Re = 60$, $Re = 100$ and $Re = 250$. Note the increasing presence of multiple modes with decreasing Reynolds number. Subsequently, only the $Re = 60$ case is analysed for multiple modes in the POD analysis and studying the LSE equation.

for the enstrophy of the investigated flow field. Qualitative features of the flow would just be the same, if we use velocity instead of vorticity fields for the POD analysis. If one defines this disturbance vorticity field as $\omega'(\boldsymbol{X}, t) = \sum_{m=1}^{M} a_m(t)\phi_m(\boldsymbol{X})$, then ϕ_m values are obtained as the eigenvectors of the covariance matrix whose elements are defined as $R_{ij} = (1/M) \int \int \omega'(\boldsymbol{X}, t_i)\ \omega'(\boldsymbol{X}, t_j) \mathrm{d}^2\boldsymbol{X}$, with $i, j = 1, 2, \ldots, M$ defined over all the collocation points in the domain. The corresponding eigenvalues give the probability of their occurrence and their sum, giving the total enstrophy of the system.

In reporting the multi-modal nature of the flow evolution by POD, we have purposely focused on the flow for $Re = 60$, for the following reason. In figure 5, we depict time histories of the lift coefficient for Reynolds numbers of 60, 100 and 250. It is evident from the figure that for $Re = 250$, there is only a single dominant mode determining the equilibrium variation of lift. In comparison, for $Re = 100$, the presence of more than one mode is evident from the displayed time variation. However, for $Re = 60$, the time history makes it abundantly clear that there are many active modes not only during the transient phase but also after the nonlinear 'saturation' of the lift coefficient.

We have analysed the flow field for $Re = 60$ by taking the same time series for three different overlapping time ranges, to account for the effects of transients on the equilibrium flow. First, eigenvalues of the dynamical system are obtained for these three cases presented in table 2. Cases A ($200 \leqslant t \leqslant 430$) and B ($350 \leqslant t \leqslant 430$) are mostly compared in the present study to highlight the roles of the transients in terms of

https://doi.org/10.1017/S0022112010001035 Published online by Cambridge University Press

POD mode number	Eigenvalues in the range Case A: $200 \leqslant t \leqslant 430$	Eigenvalues in the range Case B: $350 \leqslant t \leqslant 430$	Eigenvalues in the range Case C: $0 \leqslant t \leqslant 430$
1	1.662	2.497	0.8918
2	1.617	2.414	0.8674
3	0.484	–	0.7001
4	–	–	–
5	0.175	0.283	0.0941
6	0.174	0.280	0.0938
7	–	–	0.0830
8	–	–	–
9	–	–	0.0441
10	–	–	–
11	–	–	0.0260
12	–	–	–
13	0.042	0.037	0.0227
14	0.040	0.036	0.0217

TABLE 2. Eigenvalues in different time ranges for $Re = 60$ for flow past a cylinder.

various POD eigenmodes. Case C comprehensively includes the full time range from $t = 0$ to $t = 430$ and is used specifically to highlight the impulsive start of the flow.

In figure 6, the cumulative enstrophy content of the flow for $Re = 60$ is shown for the three cases of table 2, with five snapshots taken in a unit time interval for POD. For case C, the time range begins from an impulsive start to a state where the fluctuating component of flow variables has reached an equilibrium time-periodic state. Case B encompasses the range $200 \leqslant t \leqslant 430$, which partly includes the late-transient and the saturation stage of flow evolution, while the time interval $351 \leqslant t \leqslant 430$ contains only the equilibrium stage. Total enstrophy content during the equilibrium stage requires fewer modes for its correct description, as compared to any case that includes the transient stage. However, for all the cases, the first 15 modes account for nearly the total amount of enstrophy, with higher modes contributing insignificantly. This is the reason for including only the first 14 POD modes in table 2. We have ordered the modes in figure 6 in a numerical sequence, with blanks to indicate missing modes. This convention follows the idea in Deane *et al.* (1991), Ma & Karniadakis (2002) and Noack *et al.* (2003), which portends that the POD modes primarily form pairs, and vortex shedding in the wake is a result of interaction of these phase-shifted modes of the pairs. For example, for the flow past a cylinder, modes 1 and 2 will always form a pair with the modes roughly 90° phase apart, with an almost equal magnitude of the eigenvalues. Deane *et al.* (1991) proposed that the vortex shedding is due to interactions between the leading pair of eigenmodes $a_1(t)\ \phi_1(\boldsymbol{X})$ and $a_2(t)\ \phi_2(\boldsymbol{X})$ and defined the travelling characteristics of the vortex street. Interestingly, Noack *et al.* (2003) pointed out that the dynamics of cylinder wake are also influenced by the presence of a mode – termed by them the shift mode – that is a solitary mode without forming a pair.

When POD modes appear in pairs, they are identified here in general as regular POD modes. These POD modes have amplitude functions, whose time variation resembles the time variation of the vorticity shown in figure 2. This is displayed by the disturbance quantities following the Stuart–Landau equation. When modes appear alone and/or do not follow this type of time variation, we term them anomalous modes. Thus, anomalous modes appearing alone are always followed by a missing

https://doi.org/10.1017/S0022112010001035 Published online by Cambridge University Press

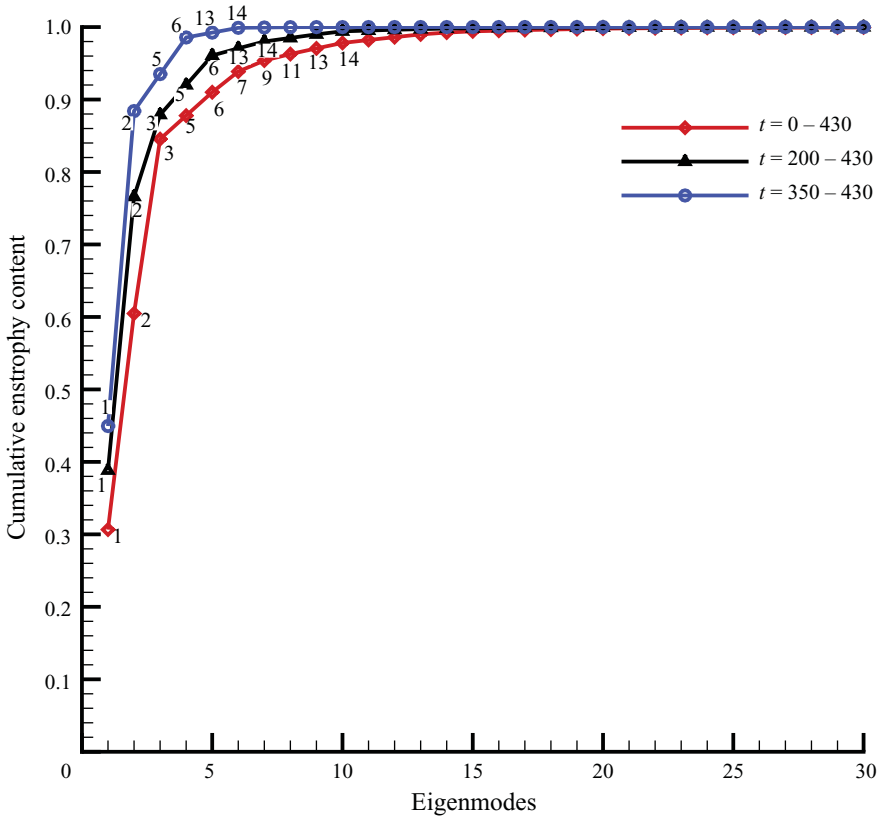


FIGURE 6. (Colour online) Cumulative enstrophy distribution among the eigenmodes for the same data set, analysed for different time ranges. The complete range for the data taken from $t = 0$ to 430 is used for the curve with rhombus symbols, data taken from $t = 200$ to 430 are shown by the curve with triangles, and data taken from $t = 350$ to 430 are shown by circles. Note that the data segments with transients require more modes for an accurate representation by POD.

mode, as shown by ϕ_3 in figure 7 for case C. This is the rationale for the nomenclature and numbering of modes used here. One encounters another type of anomalous mode which appears in pairs, but whose time variation for the corresponding amplitude function is different from that given by the Stuart–Landau equation. Eigenvalues in the various cases of table 2 are arranged and, as numbered in figure 6, become evident by looking at the eigenvectors shown in figures 7–9. We have decided upon the numbering sequence by looking at the POD results for case C. It is noted that modes 1 and 2, 5 and 6, and 13 and 14 form pairs, out of which the first two are the regular ones and the last one is anomalous. The rest of the modes belong to the first kind of anomalous mode. Modes form a pair when the eigenvalues are close to each other and the eigenvectors show a clear resemblance with a phase shift of 90°. Additionally, one can also note pairing by looking at the time variation of POD amplitude functions, as shown later.

In figure 7, eigenvectors for case C are plotted with (ϕ_1, ϕ_2) and (ϕ_5, ϕ_6) representing regular modes and the alternating vortical structures in the wake indicating the above-mentioned phase shift noted in the equilibrium flow. However, the modes (ϕ_{13}, ϕ_{14}) represent the anomalous mode of the second kind. Although the rest of the eigenvectors including ϕ_3 constitute anomalous modes of the first kind, similarity

https://doi.org/10.1017/S0022112010001035 Published online by Cambridge University Press

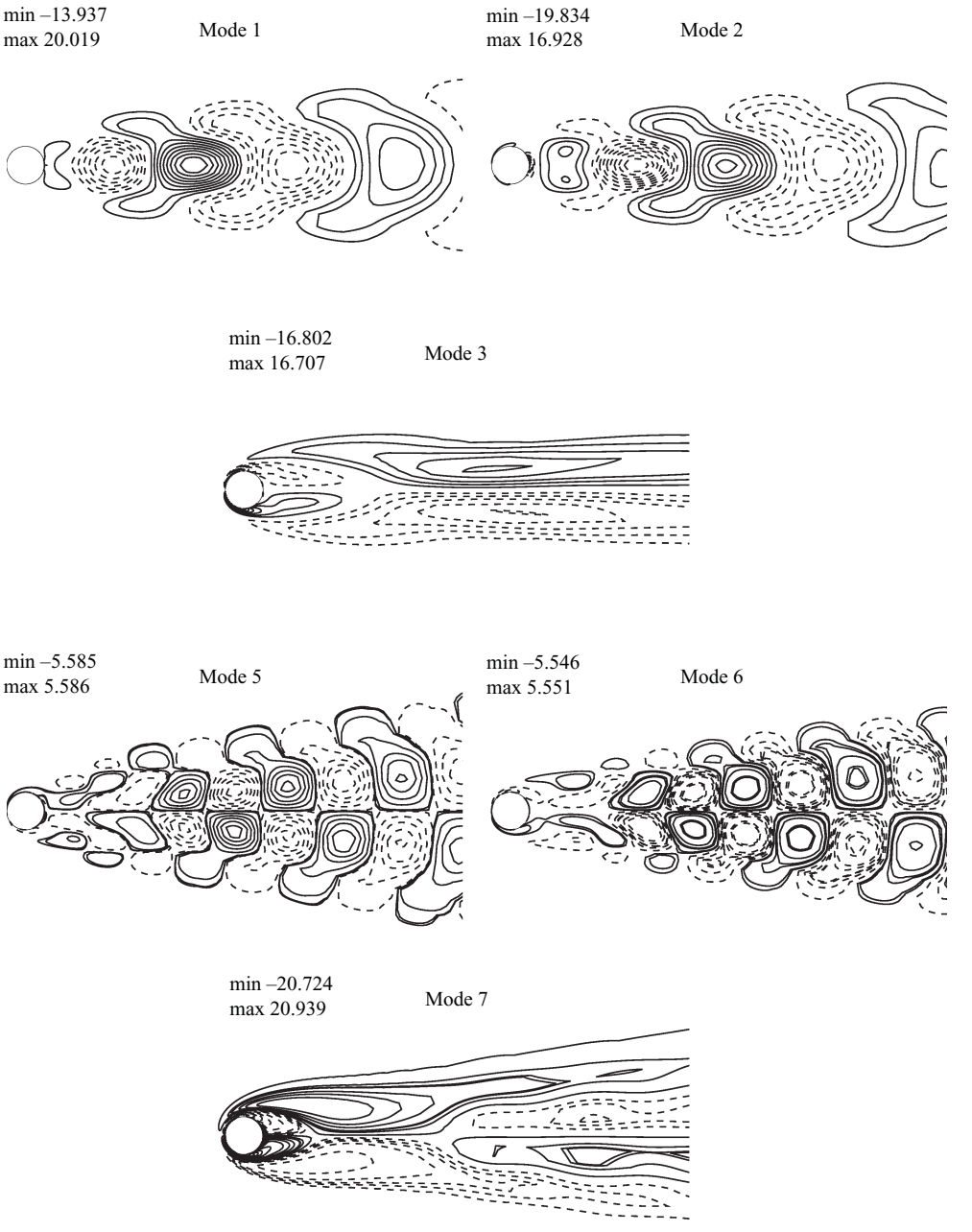


FIGURE 7. For caption see facing page.

between this type of mode with the shift mode of Noack *et al.* (2003) is noted below. For case C, we note the presence of four such anomalous modes of the first kind.

In figure 8, the eigenvectors for case A are shown and the same set of regular pairs, as indicated in table 2 by the eigenvalues, can be seen. This case is characterized by the presence of transients in part, along with the equilibrium phase of the disturbance growth. One notes the presence of an anomalous mode of the first kind (ϕ_3) and an anomalous mode of the second kind represented by (ϕ_{13}, ϕ_{14}). The regular pairs

https://doi.org/10.1017/S0022112010001035 Published online by Cambridge University Press

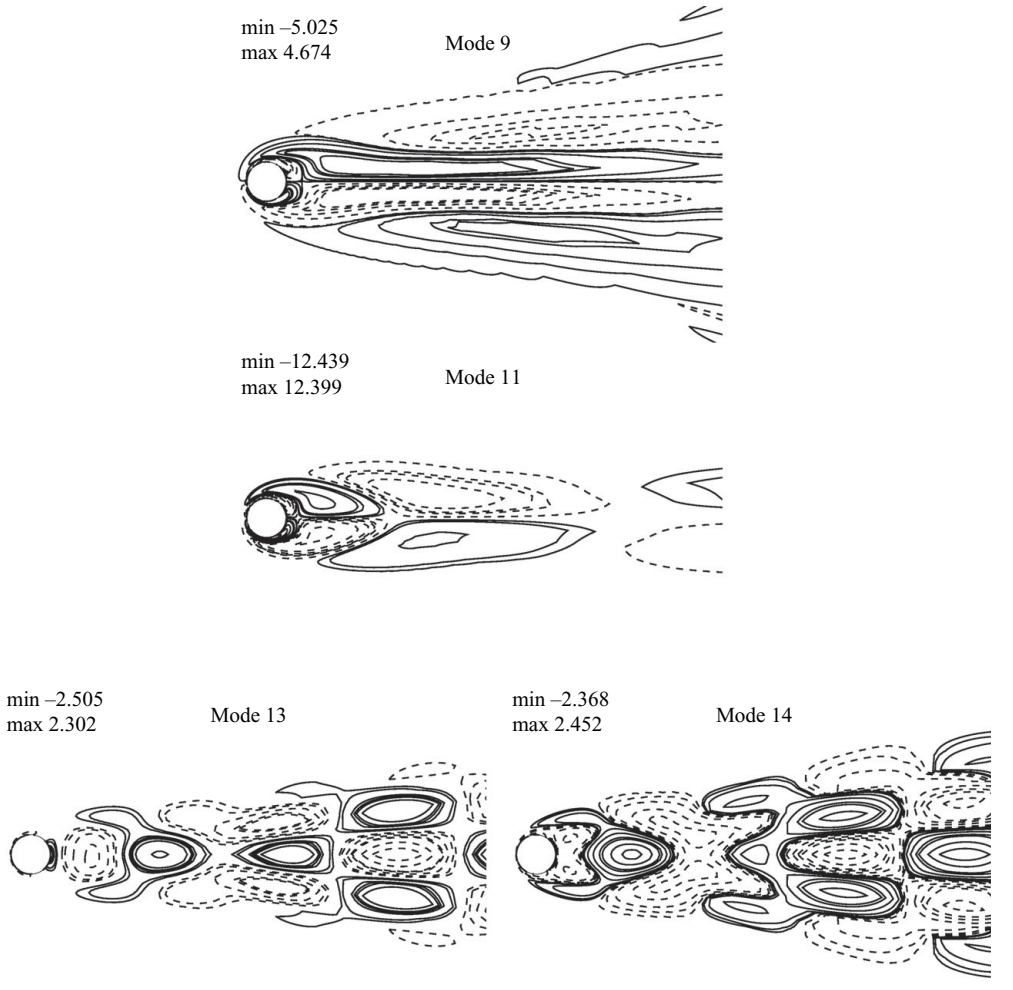


FIGURE 7. Leading eigenfunctions for the data set from $t = 0$ to 430 for $Re = 60$ following an impulsive start. Modes 1 and 2, along with modes 5 and 6, form regular pairs. Modes 3 and 7 are anomalous modes of the first kind that appear without forming pairs. Modes 13 and 14 constitute anomalous modes of the second kind, and modes 9 and 11 are anomalous modes of the first kind.

(ϕ_1, ϕ_2) and (ϕ_5, ϕ_6) define the periodic wake. The absence of early transient effects in this shorter time interval $200 \leqslant t \leqslant 430$ is characterized by a smaller number of anomalous modes of the first kind. The anomalous modes of the first kind represent essentially the transient effects.

For case B of table 2, the flow in contrast is solely in the equilibrium phase without transients, and this shows up by the presence of only three pairs of regular modes, as also seen in the eigenvector plots of figure 9. The utility of the POD analysis with accurate DNS results is clear in the present exercise, as noted by the total absence of anomalous modes. From figure 6, it is clear that these six non-trivial POD modes account for more than 99 % of total enstrophy.

The nomenclature scheme is further explained by figure 10, where computed amplitude functions ($a_j(t)$) are plotted as functions of time for case C. These are calculated from the DNS data and the obtained eigenvectors shown in figures 7–9.

https://doi.org/10.1017/S0022112010001035 Published online by Cambridge University Press

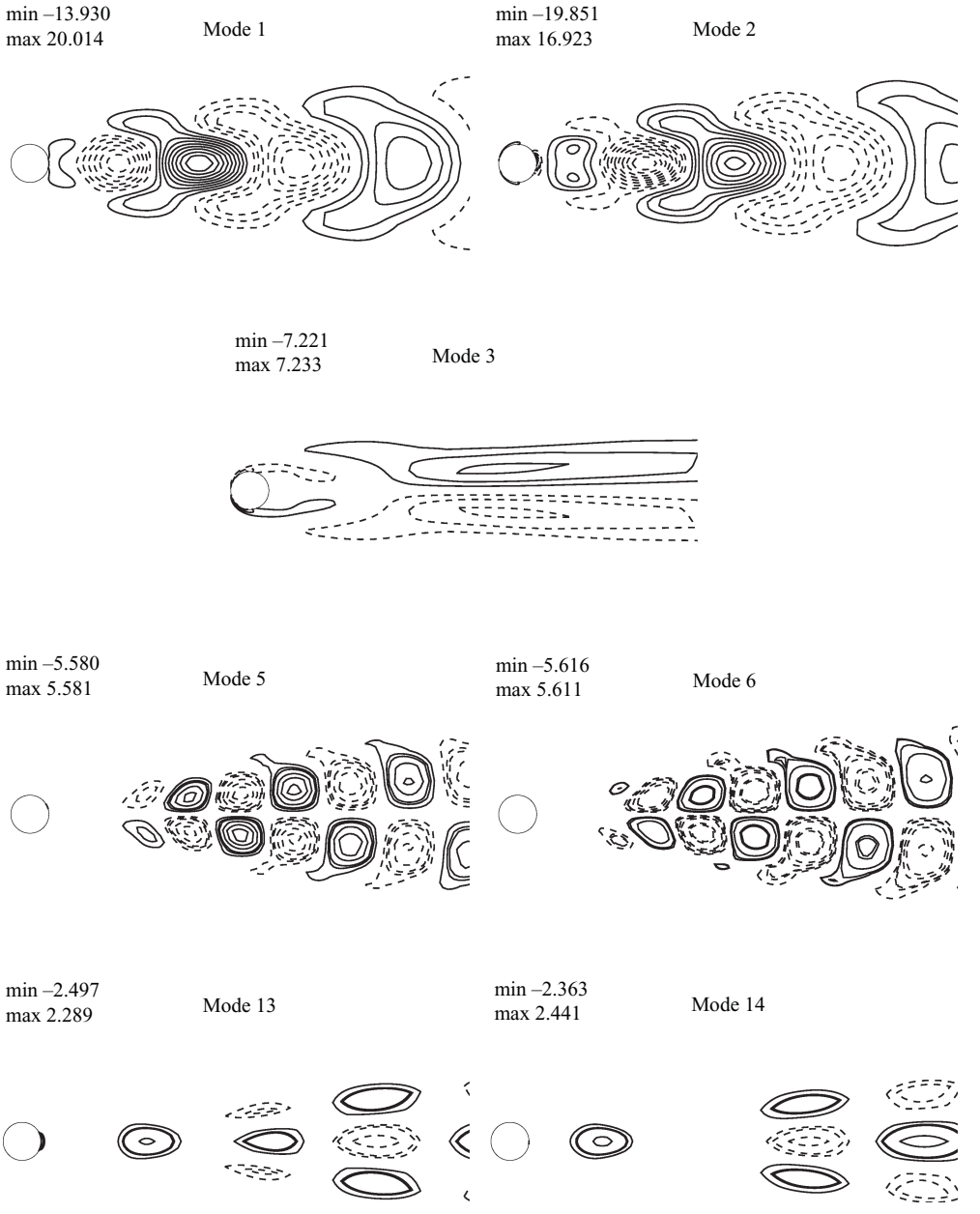


FIGURE 8. Eigenfunctions for the data set from $t = 200$ to 430 for $Re = 60$ following an impulsive start. Modes 1 and 2, along with modes 5 and 6, form regular pairs. Mode 3 is an anomalous mode of the first kind. Modes 13 and 14 constitute anomalous modes of the second kind.

It is clear from table 2 that the numerical precedence of a mode over others implies a higher contribution of that mode to the total enstrophy. The near-equality of magnitudes of successive eigenvalues indicates the formation of regular pairs and/or pairs of the anomalous mode of the second kind, while isolated modes are identified as the anomalous mode of the first kind (as seen e.g. from the third eigenvalue for cases

https://doi.org/10.1017/S0022112010001035 Published online by Cambridge University Press

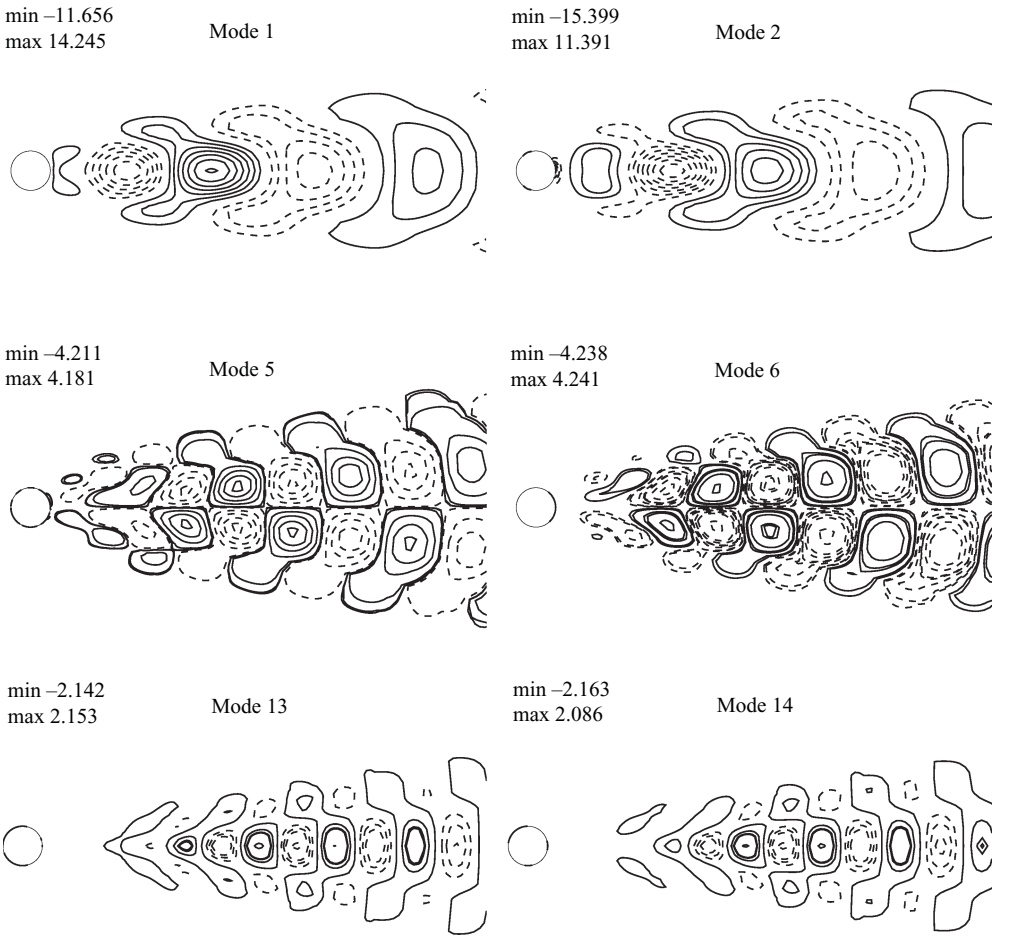


FIGURE 9. Leading eigenfunctions for the data set from $t = 350$ to 430 for $Re = 60$. All the modes form orthogonal pairs; note the absence of the anomalous modes in this case. Number and ordering of the modes are discussed in the text.

A and C in table 2). However, one cannot distinguish between regular and anomalous modes of the second kind by looking only at the eigenvalues. For this purpose, one needs to look at the amplitude functions as evaluated from the DNS data. The amplitude functions of POD modes for case C are plotted in figure 10. This figure helps in easy identification of both types of anomalous modes. While it is easy to understand the trend of the time variation of paired modes at early times as the disturbance grows from zero, it is not so for the anomalous modes of the first kind, for which the amplitude functions vary rapidly in the transient stage. To generate POD amplitude functions from the governing Navier–Stokes equation is not easy, as it amounts to solving a set of stiff differential equations (even when pressure terms are neglected, as in Deane *et al.* 1991 and Noack *et al.* 2003). The stiffness of the governing differential equations for amplitude functions involving multi-modal interactions is revisited in the next section with respect to the developed LSE equations. In figure 10, the anomalous modes of the first kind show rapid excursion during the transient stage – as seen clearly for a_3. The same is true for a_7, a_9 and a_{11}. While the amplitudes for a_7, a_9 and a_{11} are much higher as compared to a_3 in these plots, it is the third eigenmode

https://doi.org/10.1017/S0022112010001035 Published online by Cambridge University Press

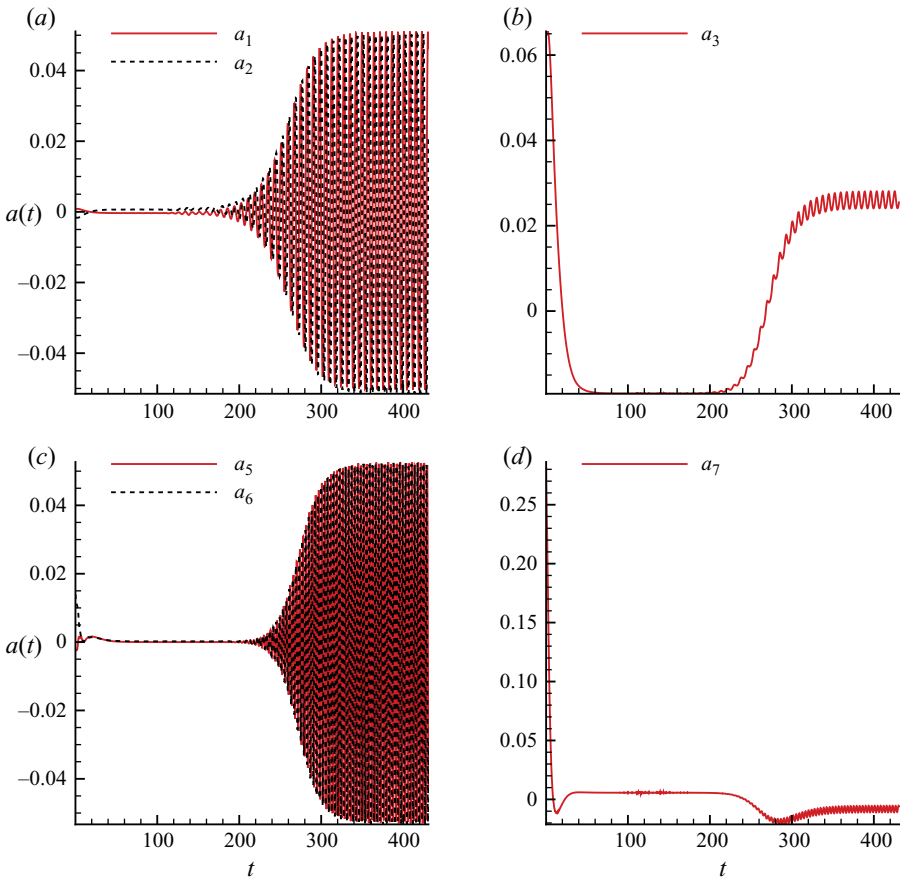


FIGURE 10. For caption see facing page.

that dominates the transients. This is understood from the relative magnitudes of eigenvalues and is discussed below with respect to (5.1) and (5.2).

The third eigenmode (ϕ_3) shown in figures 7 and 9 has been called the anomalous mode of the first kind and a similar mode in Noack *et al.* (2003) has been called the shift mode, shown in figure 7 therein. The shift mode is an attribute of the variation of the flow in a slow time scale as these 'modes can be considered as travelling waves on a slowly varying shift mode in the downstream direction' with two symmetrically placed vortices about the wake centreline. While we have obtained the anomalous mode of the first kind directly from the POD of DNS data, the shift mode was obtained differently. In Noack *et al.* (2003), 100 snapshots were taken uniformly over a single time period defined by the Strouhal frequency. Thus, in analysing the data for the shift mode, data were sampled that did not span over a full time period of the shift mode variation. In our analysis, we have sampled data over a large number of time periods (corresponding to the Strouhal frequency) – even for case B we have taken more than eight such time periods. The shift mode in Noack *et al.* (2003) has been interpreted to be present at all times. However, our analysis and the data in figures 7 and 8 show the anomalous modes of the first kind to be effectively transient in nature, as they are not seen in case B.

https://doi.org/10.1017/S0022112010001035 Published online by Cambridge University Press

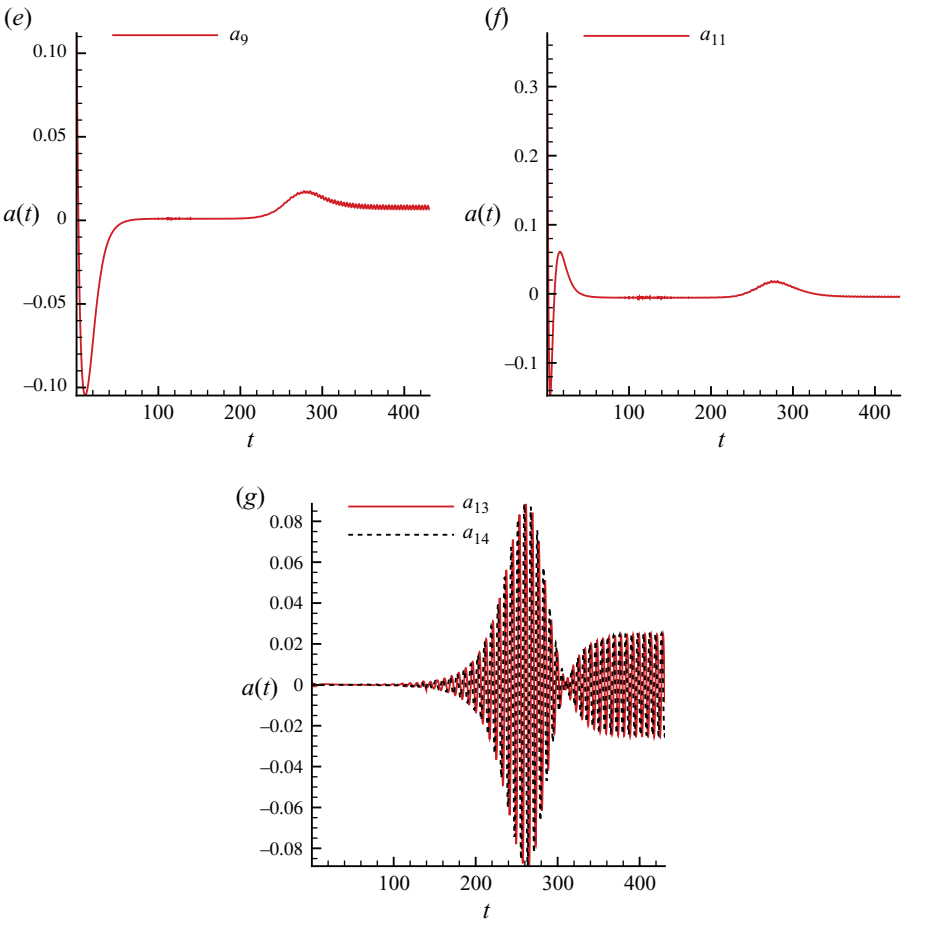


FIGURE 10. (Colour online) Time-dependent amplitude functions of the POD modes of figure 7 shown for $t = 0$ to 430. Note that a_1–a_2, a_5–a_6 and a_{13}–a_{14} form pairs, while a_3, a_7, a_9 and a_{11} do not form pairs corresponding to an anomalous mode of the first kind. The pair a_{13}–a_{14} does not follow the time variation given by either the Stuart–Landau or the LSE equations, and is an anomalous mode of the second kind.

The shift mode in Noack *et al.* (2003) was constructed as a 'mean-field correction' – equal to $(u_0 - u_s)$, where u_0 is the time-averaged solution of the unsteady Navier–Stokes equation and u_s is the solution of the steady Navier–Stokes equation. Using a Gram–Schmidt procedure, the shift mode was obtained from the 'mean-field correction'. For case A, a_{17} and a_{28} appear as isolated modes as revealed by the POD analysis. When POD modes were calculated using 20 snapshots in unit time interval for $Re = 60$ case, we did not note more than four anomalous modes of the first kind for case *A*. Rarity of such modes provides adequate reason to call them anomalous modes, whose properties are further investigated in this paper. Higher modes contribute trace amounts of enstrophy, and pairings of these are not easily seen in eigenvector plots, although eigenvalues indicate pairing. Corresponding eigenvectors are essentially at the numerical noise levels of any calculations and display no coherence.

Pairing of modes with a phase shift of 90° suggests the following connection between the POD modes with the amplitudes and eigenfunctions in (3.1) for the instability

https://doi.org/10.1017/S0022112010001035 Published online by Cambridge University Press

LSE mode number	Normalizing coefficient (ϵ_i) $[200 \leqslant t \leqslant 430]$	Normalizing coefficient (ϵ_i) $[350 \leqslant t \leqslant 430]$
1	0.77406	0.88453
2	0.11425	0
3	0.08238	0.10140
4	0.01935	0.01314
5	0.00993	0.00091

TABLE 3. Normalization coefficients for instability modes in different time ranges for $Re = 60$.

modes as

$$A_j(t) = \epsilon_j[a_{2j-1}(t) + \mathrm{i}\, a_{2j}(t)], \tag{5.1}$$

$$f_j(\boldsymbol{X}) = \frac{1}{2\epsilon_j}[\phi_{2j-1}(\boldsymbol{X}) - \mathrm{i}\,\phi_{2j}(\boldsymbol{X})], \tag{5.2}$$

where ϵ_j $[= (\lambda_{2j-1} + \lambda_{2j})/\sum_{l=1}^{N} \lambda_l]$ provides the weight of the jth instability mode in contributing to the total enstrophy. Thus, (a_1, a_2) constitute the real and imaginary parts of A_1 and (a_5, a_6) constitute A_3 and so on, for the eigenmodes appearing as pairs. However, A_2 has only one component for the eigenvectors shown in figure 7. Furthermore, a_7 forms A_4 and a_9 constitutes A_5, and so on. The POD amplitude modes in lower-case are thus related to the instability amplitude functions indicated by A_j, and we will call the latter the LSE modes as used in (6.1) to estimate the nonlinear interaction. To our knowledge, this approach of relating POD eigenmodes with the stability eigenmodes has not been done before and is attempted here for the first time. In table 3, the normalization coefficients (ϵ_j) for the amplitudes of the stability modes (A_j) are given, which are used in developing the LSE equations in the next section.

In figure 9, leading POD eigenmodes for the data in the range $351 \leqslant t \leqslant 430$ clearly show the absence of anomalous mode of the first kind. All the modes present form pairs, which are responsible for the periodicity of the flow from this time onwards. In figures 8 and 9, while A_1 and A_3 contribute to overall dynamics in an unequal measure (as noted in figure 6), their actions are also not in the same spatial region of the wake. The first instability mode A_1 is present globally with the dynamic range (as indicated by the minimum and maximum values of vorticity in the figures) that is almost three times that indicated for A_3. The other important difference between the A_1 and A_3 modes relates to the fact that the latter becomes significant only after a distance of a few diameters in the wake, as shown in figure 9. The role of the first anomalous mode can also explain the success of flow control in Strykowski (1986), Strykowski & Sreenivasan (1990) and Dipankar *et al.* (2007). In these references, the problem of controlling the wake of a cylinder by a smaller control cylinder in the near wake was investigated. It was noted that the control was effective when the control cylinder was placed in a region that resembles the near-wake contours of ϕ_3 in figure 7. We note that apart from symmetry about the wake centreline, the exact shape of the shift mode of Noack *et al.* (2003) and the anomalous mode (ϕ_3) of figure 7 are distinctly different. The location, size and shape of the anomalous eigenvector in figure 7 define the active region for the control cylinders in Strykowski & Sreenivasan (1990) better, as compared to the shift mode. Physically, when the control cylinder is placed in this patch, it creates a separation bubble of its own, which corresponds to a very

https://doi.org/10.1017/S0022112010001035 Published online by Cambridge University Press

low-Reynolds-number flow. Within this bubble, diffusion is significantly active and thus damps disturbances and, in effect, weakens A_1. Such control is effective only up to a certain Reynolds number, because of the change in mode shape with Re for ϕ_3 and the fact that even if one controls the near-wake mode A_1, A_3 can still destabilize the flow.

One of the strongest points of the present analysis is the accuracy with which the Navier–Stokes equation is calculated that allows us to capture the anomalous modes directly by POD. To understand the properties of the two different types of identified anomalous modes, we have obtained the amplitude functions by noting that the computed vorticity at the point R (defined in figure 2) in terms of the POD modes is $\omega'_R = \sum_j [a_{2j-1}(t)\phi_{2j-1}(x_R, y_R) + a_{2j}(t)\phi_{2j}(x_R, y_R)]$. Thus, using the eigenfunctions of figure 7, amplitude functions for $Re = 60$ are obtained and shown as a function of time in figure 10. Here, a_1 and a_2 form a pair and are phase-shifted by $\pi/2$, with respect to each other. Time variation of this regular pair is similar to that shown in figure 2 for vorticity, which can be explained by the Stuart–Landau equation (3.2). We also note that (a_5, a_6) corresponds to regular POD mode, with the time variation given by the Stuart–Landau equation. The second type of anomalous modes is seen in figure 10, corresponding to a_{13} and a_{14}. Although these two amplitude functions appear in pairs, their time variation is atypical of that given by the Stuart–Landau model. Note that the second anomalous mode achieves its maximum where the first anomalous mode has a negligible value. The instability portrait is obtained where the initial disturbance growth is triggered by A_2 due to its relatively higher contribution. This is evident from the relative amplitudes of a_3 *vis à vis* a_1 to a_6 in figure 9.

6. Landau–Stuart–Eckhaus equation

The Stuart–Landau equation (3.2) is incapable of explaining the discontinuity in the A_e versus Re curve, implying the inadequacy of considering only the nonlinear self-interaction. In the present work, we will attempt to explain the discontinuous variation with the help of a new equation, based on the eigenfunction expansion process of Eckhaus (1965), replacing (3.2) and (3.3). In this approach (Drazin & Reid 1981), the instability amplitude equation is given by

$$\frac{\mathrm{d}A_j}{\mathrm{d}t} = s_j A_j + \sum_{k=1}^{M} N_j(A_k), \tag{6.1}$$

where the last term accounts for the nonlinear interactions among all the M modes, including self-interaction. Eckhaus (1965) introduced the eigenfunction expansion in a Galerkin method to yield the complex amplitude equation, including multi-modal nonlinear interaction terms that also incorporate the self-interaction term of (3.2).

Since this equation is more generic and includes the Stuart–Landau equation as a special case, we will refer to (6.1) as the LSE equation – mindful of the basic idea of incorporating multi-modal interactions, which are completely absent in the Stuart–Landau equation. We are not aware of any other efforts where the LSE equation has been used to track instability of the flow past bluff bodies. In (6.1), the term $N_j(A_k)$ includes the nonlinear actions of all modes on the jth mode, including the self-interaction term. Eckhaus (1965) suggested that the nonlinear interaction term be given by $N_j(A_k) = A_j|A_k|^2$. In the actual flow past a circular cylinder, there is more than one mode that plays a major role in deciding the flow instability.

https://doi.org/10.1017/S0022112010001035 Published online by Cambridge University Press

The role of multiple POD modes in contributing to the actual signal is seen in figure 11, where the computed data at R ($x_R = 0.5044$, $y_R = 0$) are plotted and compared with the reconstructed results from the POD analysis for case A. Figure 11(a) compares the DNS data with the reconstructed signal using the POD modes 1, 2, 5 and 6. Reconstruction using these first two regular pairs of POD modes reveals poor agreement during the disturbance growth stage. In contrast, when the anomalous mode (POD modes 13 and 14) is added for reconstruction, a significant improvement is noted during the growth stage as well, shown in figure 11(b). It is also noted in figure 11(a) that retaining only the first two regular pairs actually overestimates the solution in comparison to the DNS data during the growth phase, while underestimating it in the nonlinear saturation stage. Thus, it is seen that there are multiple modes that are active during the growth and nonlinear saturation stages in varying degrees. In studying flow instability by the Stuart–Landau equation, one makes the assumption that there is only one single dominant mode dictating the instability and its nonlinear saturation. Even if one makes the allowance that the Stuart–Landau equation can be applied to different modes (as in the normal mode analysis), this places a strong restriction on these modes to act independently, during the nonlinear stage. An alternative to this was theoretically proposed by Eckhaus (1965) via an eigenfunction expansion procedure, but has not been studied before for this flow.

In performing multi-modal analysis, one needs the modal amplitudes used in (6.1). The unique feature of the present approach is to link the instability mode amplitudes in the LSE equation with the POD eigenmodes. The actual model for the nonlinear interactions and the requisite number of modes can be obtained in the following way. We note from figures 6–11 that for the flow at $Re = 60$, there are two regular pairs and two types of anomalous POD modes deciding the instability. Following the suggestions provided in Landau (1944) and Eckhaus (1965), we consider the nonlinear interactions (including self-interaction) as given in the following equations for the first and the third LSE modes of figure 7, to highlight difficulties of solving the multi-modal interaction problem. We consider the nonlinear interaction in the LSE formalism for the first two leading modes given by

$$\frac{\mathrm{d}A_1}{\mathrm{d}t} = \alpha_1 A_1 + \beta_{11} A_1 |A_1|^2 + \beta_{13} A_1 |A_3|^2, \tag{6.2}$$

$$\frac{\mathrm{d}A_3}{\mathrm{d}t} = \alpha_3 A_3 + \beta_{31} A_3 |A_1|^2 + \beta_{33} A_3 |A_3|^2. \tag{6.3}$$

It is not possible to obtain a closed-form expression for the instability amplitudes, even in the case of a system comprising only two modes while including nonlinear interactions, as given by (6.2) and (6.3). Even obtaining numerical solutions of (6.2) and (6.3) is not at all straightforward, as these constitute a set of stiff differential equations because of different orders of magnitudes for the growth rates of A_1 and A_3. This will be evident from the values of β_{ij} in these equations. We note that the POD amplitude functions of figure 10 are normalized and do not show their relative importance – while the actual normalization to be used was shown in relation (5.1). Here, we have used direct simulation data to obtain the various coefficients in (6.2) and (6.3). Using the data in table 3, one can also obtain A_1 and A_3 from DNS.

The problem of stiffness arises because of different growth rates of the fundamental solutions for A_1 and A_3, and that can be avoided by various techniques. Here, we have used the compound matrix method. This method has been developed to solve

https://doi.org/10.1017/S0022112010001035 Published online by Cambridge University Press

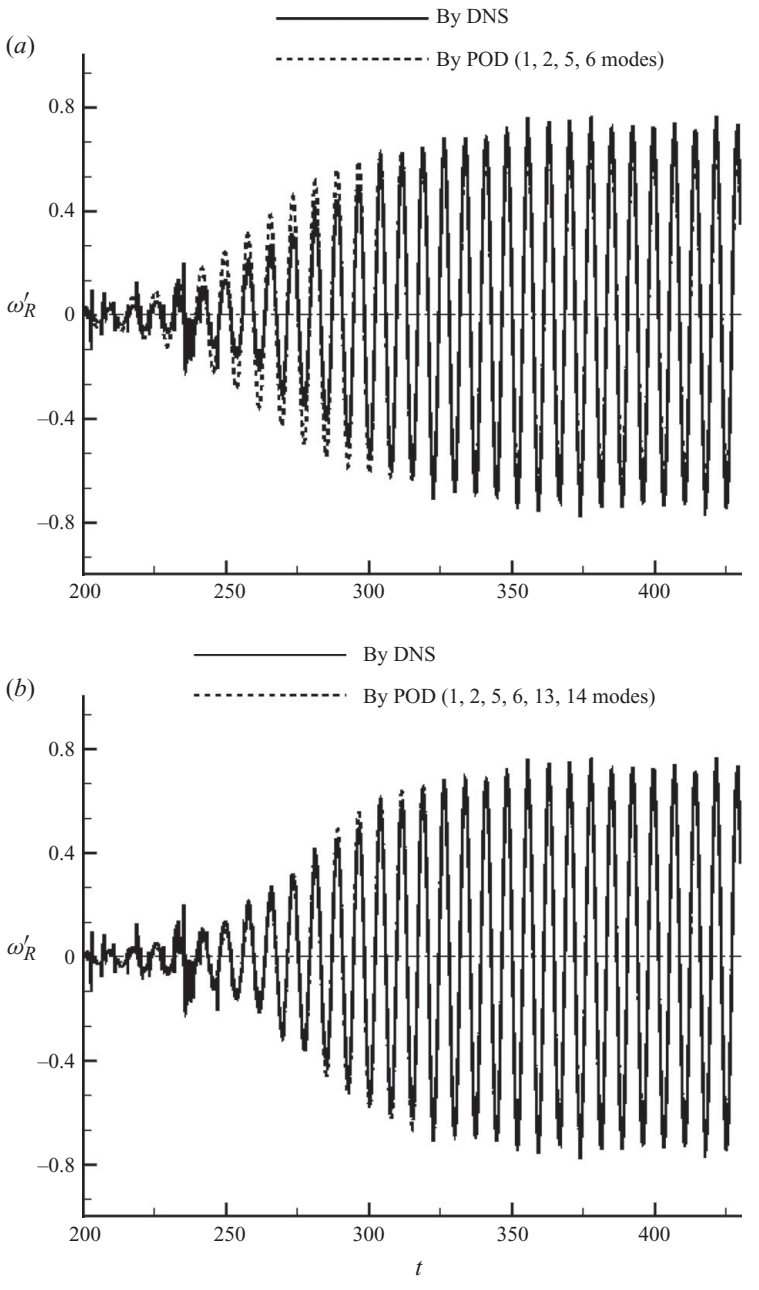


FIGURE 11. Comparison of reconstructed POD data with the DNS results for $Re = 60$ stored at a location ($x_R = 0.5044$, $y_R = 0$). (*a*) POD modes 1, 2, 5 and 6 for the reconstruction that shows overestimation in the growth phase and underestimation in the equilibrium stage. (*b*) The anomalous 13th and 14th POD modes, when added, show very good agreement with the DNS data at the growth as well as at the equilibrium stage.

stiff differential equations arising in instability problems, as discussed in Drazin & Reid (1981), Allen & Bridges (2002) and Sengupta & Venkatasubbaiah (2006). In the coupled set of equations (6.2) and (6.3), we will have two fundamental solutions with growth/decay rates differing by orders of magnitude, and that makes the differential

https://doi.org/10.1017/S0022112010001035 Published online by Cambridge University Press

equation system stiff. Compound matrix method provides an easy way to avoid this by reformulating the problem in terms of new dependent variables (as described in Drazin & Reid 1981, Allen & Bridges 2002 and Sengupta & Venkatasubbaiah 2006 and references therein). Here we transform (6.2) and (6.3) by introducing a new variable $Y = A_1 A_3$ to remove the stiffness and to obtain a single evolution equation for it:

$$Y^{-1}\frac{\mathrm{d}Y}{\mathrm{d}t} = \alpha + \beta_1|A_1|^2 + \beta_3|A_3|^2, \tag{6.4}$$

where $\alpha = \alpha_1 + \alpha_3$, $\beta_1 = \beta_{11} + \beta_{31}$ and $\beta_3 = \beta_{13} + \beta_{33}$. Equation (6.4) can be used along with the direct simulation data for $Re = 60$ to obtain the following complex coefficients: $\alpha = (0.12856, -0.34242)$, $\beta_1 = (-95.722, -1026.225)$ and $\beta_3 = (2039.764, 61376.693)$. One can clearly see that the nonlinear interaction coefficients β_1 and β_3 are of different orders of magnitude. This actually helps one realize that for the overall amplitude, the third mode (A_3) plays only a perturbative role, with the leading-order mode satisfying $\mathrm{d}A_1/\mathrm{d}t = \alpha_1 A_1 + \beta_{11} A_1|A_1|^2$ – as much as in the Stuart–Landau equation. The use of direct simulation data allows one to obtain $\alpha_1 = (0.03706, 0.75938)$, which in turn gives $\alpha_3 = (0.09149, -1.10180)$. One also obtains $\beta_{11} = (-20.330, 52.901)$ and $\beta_{31} = (-75.391, -1079.126)$. Having obtained β_{11} and α_1, (6.2) can be used to obtain the time-averaged value for $\bar{\beta}_{13} = (-3484.41, 8821.94)$. Similarly, $\bar{\beta}_{33}$ can be obtained, which also takes a large value. Such large values of nonlinear coefficients indicate that A_3 is loosely coupled in these equations with A_1.

In constructing the governing equations (6.2) to (6.4), we have purposely excluded the effects of A_2, as this anomalous mode is truly transient in contrast to that seen in figure 10, where a_3 settles down to a constant non-zero value beyond $t = 350$. Thus, the time variation for a_3 shows that the mode continues to significantly affect the dynamics beyond $t = 350$. However, this is illusory for the following reasons. First, table 3 shows that this mode in the nonlinear framework of the LSE equation (6.4) is proportional to ϵ_2^2, as compared to the first regular mode that is proportional to ϵ_1^2. This means a meagre relative contribution of 2.17 % by the anomalous mode in comparison to the first regular instability mode. Second, when the anomalous mode continues to have the same level of contribution beyond $t = 350$ in that period, the first, third and seventh instability modes collectively contribute significantly compared to A_2 in deciding the overall dynamics.

To validate the correctness of the LSE equation and its numerical solution, in figure 12, the solution obtained for (6.4) is used and compared with the solution constructed from the POD data. We have only compared the real part of Y with the POD data and the match testifies the correct correlation of the POD eigenmodes with the LSE instability modes. The imaginary part is simply phase-shifted and shows equally good comparison between the reconstruction from the solution of the LSE equation and the POD data. This process of studying multi-modal nonlinear interactions has not been attempted before, because of a misconception that POD eigenmodes can only provide approximate stability modes. The present exercise shows that one can obtain very accurate instability mode information from the POD modes. Figure 12 also testifies that the subsequent reformulation of the latter by the compound matrix method is a correct procedure to solve the resultant stiff differential equations.

https://doi.org/10.1017/S0022112010001035 Published online by Cambridge University Press

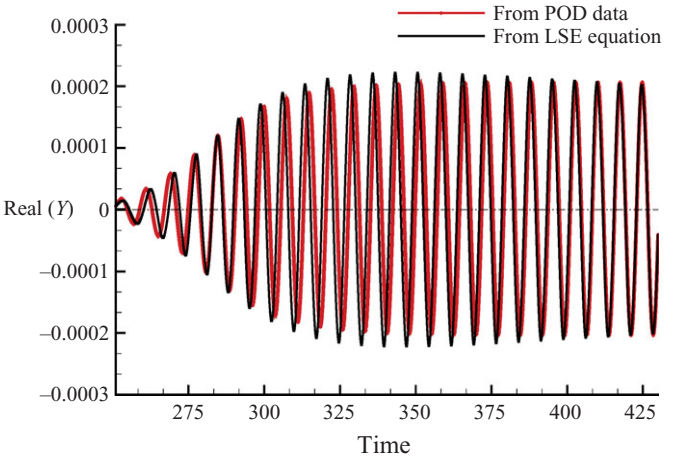


FIGURE 12. (Colour online) Comparison of the real part of $Y = A_1 A_3$ calculated using (6.4) and compared with the value of Y calculated using the POD data.

7. Summary and concluding remarks

The instability of flow past a circular cylinder is investigated following dynamical system and bifurcation theory approaches. The study reported here is completely dependent upon the high-accuracy solution of the Navier–Stokes equation in computing the time-dependent disturbance field by a dispersion-relation-preserving methodology reported in Sengupta *et al.* (2010). These computed results for the fluctuating vorticity field and the lift coefficient match extremely well with the similar trends reported in earlier experimental results of Homann (1936) and Strykowski (1986).

Some of the features of these results are delayed vortex shedding, as in Homann (1936), and a non-parabolic variation of the equilibrium amplitude of the disturbance field with Reynolds number in Strykowski (1986). Both the attributes helped us identify (i) the multi-modal nature of the flow past a circular cylinder and (ii) more than one Hopf bifurcation during flow instability, as shown in the comparisons between experimental and computational results in figures 2 and 3. With the help of the plot of computational data for the equilibrium amplitude versus Reynolds number, we have estimated three different critical Reynolds numbers, obtained using (3.5) and indicated in table 1. All the bifurcations in table 1 are for Reynolds numbers above the critical Reynolds number corresponding to the first Hopf bifurcation (as obtained in Jackson 1987, Zebib 1987, Dusek *et al.* 1994 and Morzynski *et al.* 1999). Here, attention is focused on the flow past a cylinder for $Re = 60$ that exhibits higher multi-modal features in figure 5, as compared to flows for $Re = 100$ and 250. We have focused our attention also on the second Hopf bifurcation for a Reynolds number slightly above $Re = 60$. This bifurcation can be related to the experimental observation of Homann (1936), who had reported the onset of vortex shedding for $Re \simeq 65$.

The reason for different experimental facilities (and also different numerical methods) reporting different Re_{cr} is related to the receptivity of the flow field to background disturbances during the linear temporal growth of the disturbance field for post-critical Reynolds numbers. This has been specifically demonstrated using FST models (from Sengupta *et al.* 2009*b*) in solving the Navier–Stokes equation. Specifically in figure 4, we show that the critical Reynolds number comes down from 53.29 to 49.87 for an FST level of $Tu = 0.06$ %, which was reported in Norberg (2003).

https://doi.org/10.1017/S0022112010001035 Published online by Cambridge University Press

The multi-modal nature of the flow has been investigated before using POD in Deane *et al.* (1991), Ma & Karniadakis (2002) and Noack *et al.* (2003), despite the flow featuring a single Strouhal number at post-critical Reynolds numbers. It has been pointed out in Deane *et al.* (1991) and Ma & Karniadakis (2002) that the alternate vortex shedding is a consequence of interactions between the POD modes forming pairs, with a nearly fixed phase shift of 90°. At the same time, in Noack *et al.* (2003), a new isolated mode termed the shift mode is purported to play a major role in the wake dynamics. This was obtained via an indirect procedure from a Galerkin representation. Here, principal eigenmodes have been obtained directly from POD analysis using the method of snapshots of Sirovich (1987) and a new class of modes has been reported. These have been correctly ordered and their connection to the instability modes has been established for the first time. In particular, we have identified two classes of anomalous modes, one of which appears to be similar to the shift mode, with eigenvectors bearing some qualitative resemblance. This has been termed here the anomalous mode of the first kind. However, this appears in multiple numbers, as compared to the single mode predicted in Noack *et al.* (2003), which was identified as the shift mode. Also, this shift mode was considered to be important at all times, while the anomalous mode of the first kind is seen to be significant only during the transient stage of flow evolution. The reason for this difference has been explained by linking the POD modes with the instability modes, and it is shown that at the equilibrium stage these anomalous modes have relatively lesser contributions than thought of, as discussed in § 5 and table 3. These aspects of the roles played by different modes are understood by the eigenvalues and eigenfunctions shown in figures 6–9.

Amplitude functions of the POD modes have also been obtained from DNS, which allows us to identify the anomalous modes of the second kind. Although they appear in pairs, their time variation is different from the regular pairs, which follow the Stuart–Landau equation (3.2). While they grow as regular modes to begin with, they do not achieve nonlinear saturation. Instead, they appear as wavepackets and are only important during the transient stage of flow evolution as shown in figure 10.

More importantly, multi-modal nonlinear interactions among the modes have been modelled here by the LSE equation developed in (6.1)–(6.3). These equations are totally and conceptually different from the usual Stuart–Landau equation used for the analysis of a single mode in the literature. Most importantly, in this model, mutual interactions among different modes are included, apart from the self-interaction. Eigenvalues in table 1 and eigenvectors in figure 7 identify two LSE modes to be the most dominant during the equilibrium stage. However, during the growth stage, the instability is strongly affected by the anomalous modes. In figures 7–9, two types of anomalous modes are seen, given by POD modes 3, 7, 9, 11 and 13/14.

The role of various modes is further explained by comparing the DNS data with various combinations of POD modes in figure 11. The multi-modal dynamics of flow instability are studied further using the LSE equation, and it is noted that this is much more difficult to study because of the stiff nature of the differential equations involved, as given by (6.2) and (6.3). Following the compound matrix method, a new equation is obtained, which is solved for the growth and the interaction parameters for the compound matrix variable Y. In figure 12, the reconstructed solutions of the LSE equations are compared with the POD modes and they are in very good agreement with each other. Thus, the present exercise clearly establishes the role of multiple modes and multiple Hopf bifurcations for the flow past a cylinder. This has been done using very accurate numerical solution of the Navier–Stokes equation

https://doi.org/10.1017/S0022112010001035 Published online by Cambridge University Press

without any additional modelling. Also, the interactions of the LSE modes have been established via the LSE equations and reported here for the first time.

Having been able to show the importance of multiple instability modes in determining vortex shedding behind a circular cylinder, it is natural to formulate these interactions through the LSE equations that are extensions to the Stuart–Landau equation for a single dominant mode only. Accurate direct simulations open up possibilities for the linear and nonlinear instability studies for bluff-body flows.

The authors acknowledge Professor Strykowski for permitting reproduction of materials from his thesis. Authors are also grateful for the help provided by Mr V. V. S. N. Vijay, Mr Shameem Usman and Mr Y. G. Bhumkar with codes and figures.

REFERENCES

Allen, L. & Bridges, T. 2002 Numerical exterior algebra and the compound matrix method. *Numer. Math.* **92**, 197–232.

Barkley, D. 2006 Linear analysis of the cylinder wake mean flow. *Europhys. Lett.* **75** (5), 750–756.

Batchelor, G. K. 1988 *Introduction to Fluid Dynamics*. Cambridge University Press.

Chomaz, J.-M. 2005 Global instabilities in spatially developing flows: non-normality and nonlinearity. *Annu. Rev. Fluid Mech.* **37**, 357–392.

Deane, A. E., Kevrekidis, I. G., Karniadakis, G. E. & Orszag, S. A. 1991 Low-dimensional models for complex geometry flows: application to grooved channels and circular cylinders. *Phys. Fluids* A **3**, 2337–2354.

Dipankar, A., Sengupta, T. K. & Talla, S. B. 2007 Suppression of vortex shedding behind a circular cylinder by another control cylinder at low Reynolds numbers. *J. Fluid Mech.* **573**, 171–190.

Drazin, P. G. & Reid, W. H. 1981 *Hydrodynamic Instabilities*. Cambridge University Press.

Dusek, J., Le Gal, P. & Fraunie, P. 1994 A numerical and theoretical study of the first Hopf bifurcation in a cylinder wake. *J. Fluid Mech.* **264**, 59–80.

Eckhaus, W. 1965 *Studies in Nonlinear Stability Theory*. Springer.

Giannetti, F. & Luchini, P. 2007 Structural sensitivity of the first instability of the cylinder wake. *J. Fluid Mech.* **581**, 167–197.

Golubitsky, M. & Schaeffer, D. G. 1984 *Singularities and Groups in Bifurcation Theory*. Springer.

Henderson, R. D. 1997 Nonlinear dynamics and pattern formation in turbulent wake transition. *J. Fluid Mech.* **352**, 65–112.

Holmes, P., Lumley, J. L. & Berkooz, G. 1996 *Turbulence, Coherent Structures, Dynamical Systems and Symmetry*. Cambridge University Press.

Homann, F. 1936 Einfluss grosser Zähigkeit bei Strömung um Zylinder. *Forsch. auf dem Gebiete des Ingenieurwesens* **7** (1), 1–10.

Huerre, P. & Rossi, M. 1998 Hydrodynamic instabilities in open flows. In *Hydrodynamics and Nonlinear Instabilities* (ed. C. Godreche & P. Manneville), pp. 81–294. Cambridge University Press.

Jackson, C. P. 1987 A finite-element study of the onset of vortex shedding in flow past variously shaped bodies. *J. Fluid Mech.* **182**, 23–45.

Kiya, M., Suzuki, Y., Mikio, A. & Hagino, M. 1982 A contribution to the free stream turbulence effect on the flow past a circular cylinder. *J. Fluid Mech.* **115**, 151–164.

Kosambi, D. D. 1943 Statistics in function space. *J. Indian Math. Soc.* **7**, 76–88.

Kovasznay, L. S. G. 1949 Hot-wire investigation of the wake behind cylinders at low Reynolds numbers. *Proc. R. Soc. Lond.* A **198**, 174–190.

Landau, L. D. 1944 On the problem of turbulence. *C. R. Acad. Sci. USSR* **44**, 311–315.

Landau, L. D. & Lifshitz, E. M. 1959 *Fluid Mechanics*, vol. 6. Pergamon.

Ma, X. & Karniadakis, G. E. 2002 A low-dimensional model for simulating three-dimensional cylinder flow. *J. Fluid Mech.* **458**, 181–190.

https://doi.org/10.1017/S0022112010001035 Published online by Cambridge University Press

Marquet, O., Sipp, D., Chomaz, J.-M. & Jacquin, L. 2008 Amplifier and resonator dynamics of a low-Reynolds-number recirculation bubble in a global framework. *J. Fluid Mech.* **605**, 429–443.

Morzynski, M., Afanasiev, K. & Thiele, F. 1999 Solution of the eigenvalue problems resulting from global nonparallel flow stability analysis. *Comput. Meth. Appl. Mech. Engng* **169**, 161–176.

Nishioka, M. & Sato, H. 1978 Mechanism of determination of the shedding frequency of vortices behind a cylinder at low Reynolds numbers. *J. Fluid Mech.* **89**, 49–60.

Noack, B. R., Afanasiev, K., Morzynski, M., Tadmor, G. & Thiele, F. 2003 A hierarchy of low-dimensional models for the transient and post-transient cylinder wake. *J. Fluid Mech.* **497**, 335–363.

Noack, B. R. & Eckelmann, H. 1994 A low-dimensional Galerkin method for the three-dimensional flow around a circular cylinder. *Phys. Fluids* **6** (1), 124–143.

Noack, B. R., Papas, P. & Monkewitz, P. A. 2005 The need for a pressure-term representation in empirical Galerkin models of incompressible shear flows. *J. Fluid Mech.* **523**, 339–365.

Noack, B. R., Schlegel, M., Ahlborn, B., Mutschke, G., Morzynski, M., Comte, P. & Tadmor, G. 2008 A finite-time thermodynamics of unsteady fluid flows. *J. Non-Equilib. Thermodyn.* **33**, 103–148.

Noack, B. R., Schlegel, M., Morzynski, M. & Tadmor, G. 2009 System reduction strategy for Galerkin models of fluid flows. *Intl J. Numer. Methods Fluids* **63** (2), (Jan. 2011) doi:10.1002/fld.2049.

Norberg, C. 2003 Fluctuating lift on a circular cylinder: review and new measurements. *J. Fluids Struct.* **17**, 57–96.

Provansal, M., Mathis, C. & Boyer, L. 1987 Benárd–von Kármán instability: transient and forced regimes. *J. Fluid Mech.* **182**, 1–22.

Roshko, A. 1954 On the drag and shedding frequency of two-dimensional bluff bodies. *NACA Tech Note* 3169.

Schlichting, H. 1987 *Boundary Layer Theory*. McGraw-Hill.

Sengupta, T. K., Bhumkar, Y. & Lakshmanan, V. 2009*a* Design and analysis of a new filter for LES and DES. *Comput. Struct.* **87**, 735–750.

Sengupta, T. K., Das, D., Mohanamuraly, P., Suman, V. K. & Biswas, A. 2009*b* Modelling free-stream turbulence based on wind tunnel and flight data for instability studies. *Intl J. Emerging Multidiscip. Fluid Sci.* **1** (3), 181–201.

Sengupta, T. K. & Dey, S. 2004 Proper orthogonal decomposition of direct numerical simulation data of by-pass transition. *Comput. Struct.* **82**, 2693–2703.

Sengupta, T. K., Sircar, S. K. & Dipankar, A. 2006 High accuracy schemes for DNS and acoustics. *J. Sci. Comput.* **26** (2), 151–193.

Sengupta, T. K., Suman, V. K. & Singh, N. 2010 Solving Navier–Stokes equation for flow past cylinders using single-block structured and overset grids. *J. Comput. Phys.* **229** (1), 178–199.

Sengupta, T. K. & Venkatasubbaiah, K. 2006 Spatial stability for mixed convection boundary layer over a heated horizontal plate. *Stud. Appl. Math.* **117**, 265–198.

Sipp, D. & Lebedev, A. 2007 Global stability of base and mean flows: a general approach and its applications to cylinder and open cavity flows. *J. Fluid Mech.* **593**, 333–358.

Sirovich, L. 1987 Turbulence and dynamics of coherent structures. Part I Coherent Structures, Part II Symmetries and Transformations and Part III Dynamics and Scaling. *Q. Appl. Math.* **45**, 561–590.

Sreenivasan, K. R., Strykowski, P. J. & Olinger, D. J. 1987 Hopf bifurcation, Landau equation and vortex shedding behind circular cylinders. In *Forum on Unsteady Flow Separation* (ed. K. N. Ghia), pp. 1–13. ASME.

Strykowski, P. J. 1986 The control of absolutely and convectively unstable shear flows. PhD thesis, Yale University.

Strykowski, P. J. & Sreenivasan, K. R. 1990 On the formation and suppression of vortex shedding at low Reynolds number. *J. Fluid Mech.* **218**, 74–107.

Stuart, J. T. 1960 On the nonlinear mechanics of wave disturbances in stable and unstable parallel flows. Part 1. The basic behaviour in plane Poiseuille flow. *J. Fluid Mech.* **9**, 353–370.

Tadmor, G., Lehmann, O., Noack, B. & Morzynski, M. 2010 Mean field representation of the natural and actuated cylinder wake. *Phys. Fluids* **22** (3), 034102-1 to 22.

https://doi.org/10.1017/S0022112010001035 Published online by Cambridge University Press

Thompson, M. C. & Le Gal, P. 2004 The Stuart–Landau model applied to wake transition revisited. *Eur. J. Mech.,* B/*Fluids* **23**, 219–228.

Tordella, D. & Cancelli, C. 1991 First instabilities in the wake past a circular cylinder: comparison of transient regimes with Landau's model. *Meccanica* **26**, 75–83.

Van der Vorst, H. A. 1992 Bi-CGSTAB: a fast and smoothly converging variant of Bi-CG for the solution of non-symmetric linear systems. *SIAM J. Sci. Stat. Comput.* **12**, 631–644.

Watson, J. 1960 On the nonlinear mechanics of wave disturbances in stable and unstable parallel flows. Part 2. The development of a solution for plane Poiseuille flow and for plane Couette flow. *J. Fluid Mech.* **9**, 371–389.

Williamson, C. H. K. 1989 Oblique and parallel modes of vortex shedding in the wake of circular cylinder at low Reynolds numbers. *J. Fluid Mech.* **206**, 579–627.

Zebib, A. 1987 Stability of viscous flow past a circular cylinder. *J. Engng Math.* **21**, 155–165.

https://doi.org/10.1017/S0022112010001035 Published online by Cambridge University Press